國立清華大學

材料科學工程研究所

博士論文

鐵錳底層對於鐵鉑合金之序化、表面形貌以及磁性行為之影響

Effect of PtMn underlayer on ordering, morphology and magnetic behavior of FePt

研究生：蔣肇謙
Student: Chao-Chien Chiang
指導教授：賴志煌 教授
Advisor: Prof. Chih-Huang Lai

中華民國 一百 年 六 月

Abstract

The ordering temperature of FePt films grown on PtMn underlayers was reduced due to phase transformation of the PtMn $L1_0$ phase. The in-plane coercivity of 10 nm FePt on 50 nm PtMn underlayers was 7688 Oe after annealing at 325°C. An exchange field of 554 Oe was also observed, which indicates that PtMn may not only induce the ordering of FePt at a reduced temperature, but also may provide extra anisotropy.

We then use MgO (001) substrates to grow perpendicular PtMn/FePt films. The presence of PtMn eliminates the strip domains, observed in (001) FePt directly grown on MgO, and forms special rectangular domains. As the thickness of the FePt increases, the switching behavior of samples with PtMn underlayer changes from rotation dominant type to the domain wall motion dominant type. On the contrary, samples without PtMn layer show domain wall motion dominant type for all thickness we studied. As the thickness of FePt reaches 50nm, sample shows strong vertically correlated magnetization reversal due to the large static magnetic energy. The coercivity of all samples are enhanced by inserting the PtMn layer. The enhanced coercivity is related to the changes of the morphology and exchange coupling between antiferromagnetic PtMn and FePt. Moreover, we found that the PtMn/FePt samples form special graded anisotropy profile in which the soft layer is in the middle of the magnetic layer. Therefore, the PtMn underlayer can induce the ordering of FePt and is also a good underlayer for perpendicular growth of FePt. Moreover, the diffusion of Mn from PtMn makes the FePt become a graded media, in which a soft layer is formed and helps the magnetization reversal of the FePt layer.

摘 要

本論文主要研究錳白金底層對於鐵白金合金性質之影響。在第一個部分我們發現錳白金底層能夠促進鐵金之低溫相變化。我們將錳白金底層與鐵白金一同鍍製在二氧化矽的基板上，我們發現厚度為10奈米的鐵白金長在50奈米的錳白金底層上在325°C 退火處理後，水平的矯頑磁場為7688 Oe。另外，我們也觀察到 554 Oe 的交換場，這表示錳白金除了能夠促進鐵白金的低溫相變之外，還提供了額外的異向性能來增加鐵白金的矯頑磁場。

之後，我們利用氧化鎂(001)的基板來成長具有垂直異向性的鐵白金薄膜。我們發現，利用錳白金底層能夠消除單純鐵白金長在氧化鎂基板上所出現的長條狀的磁域，並形成特殊的方塊型磁域。當成長在錳白金底層的鐵白金的厚度由12.5奈米逐漸增厚之後，其磁性翻轉的機制由原本的回轉模式為主轉變成由磁域壁移動所主導的翻轉機制。然而在沒有錳白金底層的樣品，我們發現其翻轉機制都是由磁域壁移動所主導。所有鐵白金的矯頑磁場都因為加了錳白金的底層而上升，這是因為錳白金的底層改變了鐵白金的成長機制進而改變其表面形貌，另外錳白金也提供了一個額外的異向性能，因此改變了鐵白金的矯頑磁場。

最後我們研究錳白金以及鐵白金這個雙層結構縱向的異向性能的分佈，我們發現由於錳的擴散以及反鐵磁性的錳白金提供額外異向性的緣故，此一雙層結構呈現中間軟而上下硬的異向性分佈。此為一漸進式媒體所需要的結構。

Acknowledgement

不知不覺，已經在清大度過了十幾個寒暑。感謝爸媽讓我可以這樣專心一致的只顧學業而不需要煩惱其他的事情。感謝我的指導老師賴志煌教授，拼命的督促我的實驗，忍受我這個慢郎中好多年。感謝金重勳教授、曾院介教授、蔡佳霖教授以及歐陽浩教授對於我的論文的指教與批評，讓我受益良多。

博士班這幾年，大部份的時候都花在實驗室，能夠認識這些好夥伴一起奮鬥是我的福氣。謝謝泳泓、威全、郁仁、朝成、震麟、允中、若帆、姍意、政翰、保萱和柏翔等學長，是你們帶領我並接納我成為實驗室的一員，開啓了我日後繼續研究的契機。夢嫻、勝煌還有建新，謝謝你們處處提醒我沒注意到的小地方，希望你們都一帆風順。皓程、良瑋、容蔚、偉志、如正，感謝你們這些年在實驗上互相的幫助，能夠跟你們一起同組打拼是我的榮幸。感謝武璋，陪我一起努力撐過那些維修機台不能做實驗的日子。彥鈞、家庠、國峰、鼎碩、聖傑，有你們在實驗室讓我可以在那些苦悶的日子中找到一點笑容。志宇、家豪、鼎翔，雖然跟你們認識的時間只有短短兩年，但還是很高興能夠跟你們一起畢業。

最後感謝合唱團的那一群朋友們，建欣、艾靈、劭品跟正芝等人，讓我在課業之中能有夠個地方可以喘口氣。感謝這一路上陪我一起走過的朋友們，很開心一路上有你們相伴。

Contents

List of Figures

Chapter 1

Introduction

Magnetic storage has played an important role in audio, video, and computer developments since its invention. In 1956, IBM built the first magnetic hard disk drive at a recording density of 2kbit/in^2. Till now, the pursuit of smaller, lighter, faster and larger capacity storage device still continues. However, the continued growth in areal density is limited by thermal effects known as the 'superparamagnetic effect'[1].

In the past, magnetic disk drives are based on longitudinal recording systems where the magnetization of each recorded bit lies in the plane of the disk. Data are recorded in a granular magnetic recording medium using the inductive write element of an integrated thin film write/read head. The data are read back with the giant magneto resistive sensor element which sense the stray field of the recording medium. In order to increase the recording density, the bit length and track width should be reduced. By doing so, all the relevant physical dimensions have to be changed together in the same proportion. Therefore, people tried various way, such as oriented longitudinal media[2], AFC recording media[3,4], perpendicular recording[5], thermally assisted media[6], patterned media[7], etc., to avoid the thermal decay problem. In order to increase the ther-

mal stability, the high magnetic anisotropy with low switching field material is a solution for the next generation magnetic recording media.

1.1 Motivation

As the demand for high-density recording increases, it is necessary to search for magnetic media possessing high magnetic anisotropy. The tetragonal FePt $L1_0$ phase exhibiting high magnetocrystalline anisotropy is one of potential candidates. Typically, as-deposited FePt films of disordered fcc phase are magnetically soft. A postannealing process at temperatures higher than 500 °C[8] is needed to develop an ordered fct $L1_0$ phase and an adequately large coercivity. Although the requisite processing temperature is not compatible with current manufacturing process, FePt is still a viable media material in the range of magnetic recording media because of the high magnetocrystalline anisotropy. Therefore, to find a way to decrease processing temperature and at the same time control the coercivity of FePt is an important task for future recording media.

1.2 Outline of the Dissertation

This chapter briefly introduces the reported researches about the evolution of recording media in recent years, and describes the motivation of choosing FePt in my studies in the dissertation. In the following chapter, I will further present the backgrounds relevant to the discussions in this dissertation. I introduced basic characteristics of FePt and some theories of anisotropy. Furthermore, I also summarized previous models established for the exchange bias in FM/AFM layers. Some important researches about the FePt are also discussed. Chapter

3 introduce the techniques which we used to fabricate and analyze our samples. In chapter 4, the reduction of FePt ordering temperature by PtMn underlayer is discussed. Chapter 5 focus on the perpendicular PtMn/FePt films and their magnetic behavior. Chapter 6 is a discussion the influence of the diffusion of Mn and the special anisotropy profile of FePt. The dissertation is summarized in Chapter 7.

Chapter 2

Background

2.1 Properties of FePt

In recent years, demand of area density of data storage has continually increased. As of now, the recording densities have reached over 100 Gbits/in^2. To reach a even higher recording density, the recording media must possess high anisotropy energy and small but magnetically isolated grains. With the reduction of the grain size of the magnetic material, the magnetization of a recorded information becomes unstable because of the superparamagnetic effect. Therefore, FePt is a suitable material which has high crystal anisotropy and good corrosion resistance.

Figure 2.1 illustrates the Fe-Pt phase diagram. There are three major equilibrium FePt solid phases in the low temperature region: (1) γ_1-Fe_3Pt phase, (2) γ_2-FePt phase and (3) γ_3-$FePt_3$ phase.

The disordered phase of $FePt_3$ phase is ferromagnetic while the ordered $L1_2$ phase is antiferromagnetic. This is because the Fe atoms are arranged on a simple cubic lattice[9]. FePt and Fe_3Pt are both ferromagnetic in ordered and disordered phase. The γ_2-FePt order phase possesses high crystal anisotropy

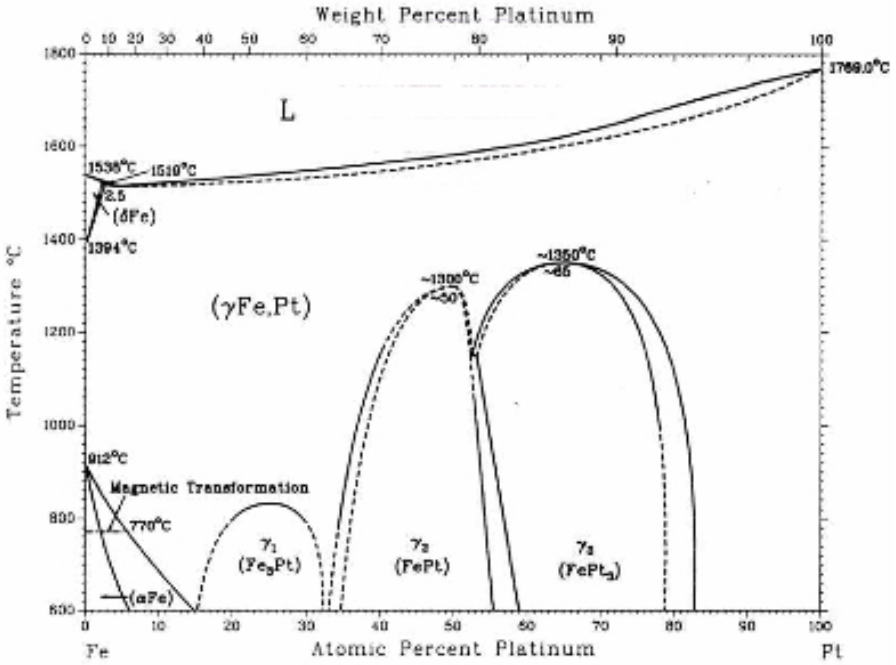

Figure 2.1: Fe-Pt equilibrium phase diagram. (Data are from Thaddeus B. Massalski et al., Binary alloy phase diagrams, Materials Park, Ohio/ASM International, 1990.)

and is what we interested in. Figure 2.2 shows the crystal structure of the ordered and disordered FePt phases. The FePt disordered phase is a face-centered cubic (A1) structure with lattice constant of 0.3816nm, and the ordered phase is a face-centered tetragonal ($L1_0$) structure with lattice constant of 0.3853nm and 0.3713nm. The equilibrium phase of FePt at low temperature is the ordered γ_2 phase, however, the as-deposit FePt thin films usually are the disordered γ phase. An annealing process which temperature is higher than 500 °C is required in order to obtain the γ_2-FePt order phase.

2.2 Anisotropy

The magnetic anisotropy, which is related to the coercivity and the switching behavior, is the direction dependence of a material's magnetic properties. A magnetically anisotropy material has a special direction in which the magnetic

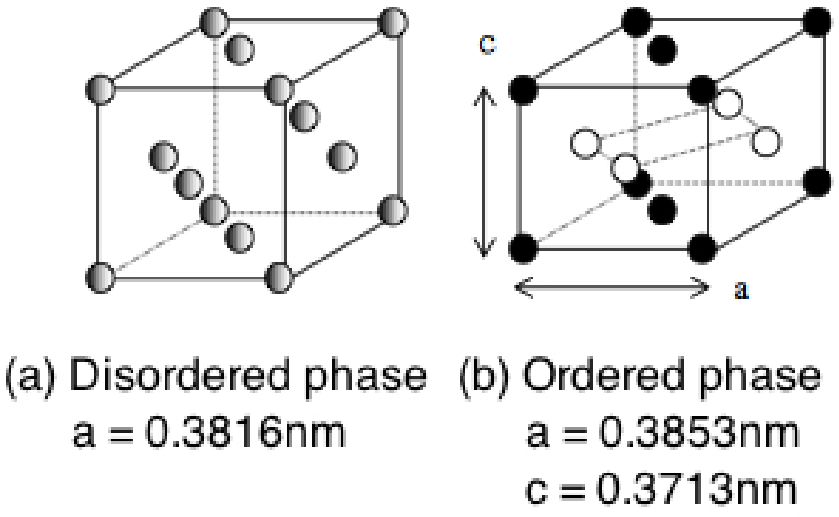

Figure 2.2: Schematic diagrams of crystal structures of 50 at % Fe-Pt alloy. (a) shows a disordered structure in which the probability of each lattice point occupied by Fe or Pt atoms are equal. (b) shows an ordered structure in which Fe and Pt atoms occupy the specific lattice points.

moment prefer to align. The energetically favorable direction is called easy axis which is determined by the sources of magnetic anisotropy listed below:

1. Magnetocrystalline anisotropy
2. Shape anisotropy
3. Magnetoelastic anisotropy
4. Exchange anisotropy

Below are brief introductions of the sources of anisotropy.

2.2.1 Magnetocrystalline anisotropy

Magnetocrystalline anisotropy is the dependence of the internal energy of a ferromagnet on the crystallographic direction of its magnetization. The spin-orbit interaction is the primary source of the magnetocrystalline anisotropy. The magnetocrystalline anisotropy energy is generally represented as an expansion in powers of the direction cosines of the magnetization. Because of time reversal symmetry, only even powers of the cosines are allowed. The non zero terms in the expansion depend on the crystal system[10]. In the case of FePt, the crystal has a single axis of high symmetry. This is called uniaxial anisotropy. The energy density for a tetragonal crystal is:

$$E/V = K_1 \sin^2\theta + K_2 \sin^4\theta + K_3 \sin^4\theta \sin 2\phi \tag{2.1}$$

The parameter K_1, often represented as K_u, has units of energy density and depends on the material, composition and temperature. The K_3 term, the one that determines the basal plane anisotropy, may vary by a constant. θ is the angle between the saturated magnetization (M_s) and the easy axis. Many models of magnetization represent the anisotropy as uniaxial and ignore higher order terms. However, if $K_1 < 0$, the lowest energy term does not determine the direction of the easy axes within the basal plane. In this case, higher-order terms are needed, and varies with the crystal system.

2.2.2 Shape anisotropy

The shape anisotropy comes from the demagnetizing field generated by the magnetization in a magnet. For the special case of ellipsoids (which includes spheres) the demagnetization field (H_d) is linearly related to the magnetization (M) by a geometry dependent constant called the demagnetizing factor

(N_d). For a uniformly magnetized sphere in a uniform magnetic field H_0 the demagnetization field is

$$H_d = H_0 - N_d M \tag{2.2}$$

In c.g.s unit system, the sum of the demagnetizing factor in all direction by Cartesian coordinate system is 4π and can be written as fellow:

$$N_x + N_y + N_z = 4\pi \tag{2.3}$$

Thus, for a perfect sphere, the demagnetizing factor N_d equals to $4\pi/3$ and for an infinite plate which has N_d equals to 4π in a direction normal to the plate and zero otherwise. Also an infinite cylinder which has N_d equals to 2π along its axis. Equation 2.2 can be generalized to include ellipsoids having principal axes in x,y, and z directions such that each component has a relationship of the form:

$$(H_d)_k = (H_0)_k - (N_d)_k M_k \tag{2.4}$$
$$k = x, y, z$$

2.2.3 Magnetoelastic anisotropy

When a stress is applied to a magnetic material, the magnetic domain may change. The easy axis direction changes by the strain energy (E_σ). In the case of a single stress σ applied on a single magnetic domain, the magnetic strain energy density can be expressed as:

$$E_\sigma = \frac{3}{2}\lambda_s \sigma \sin^2\theta \tag{2.5}$$

where λ_s is the magnetostrictive expansion at saturation, and θ is the angle between the saturation magnetization and the stressed direction. When λ_s and σ are both positive, the energy is minimum for the saturation magnetization is aligned with the stress ($\theta = 0$).

2.2.4 Exchange anisotropy

Exchange anisotropy, the exchange coupling phenomenon in the magnetic multilayers, was first discovered in partially oxidized Co particles by Meiklejohn and Bean[11,12]. Their discovery was initiated by the observation that the hysteresis loop below room temperature of nominal Co nano-particles was shifted along the field axis after cooling in an applied field. It was subsequently established that the particles had been partially oxidized to CoO, which is an antiferromagnet. Thus, the particles could be considered to consist of a core of single domain Co and a shell of antiferromagnetic CoO. A compact of these particles was then cooled in a magnetic field to 77K, and its hysteresis loop was measured at that temperature. As shown in figure 2.3 , the hysteresis loop of the partially oxidized Co particles is not symmetrical about the origin but is shifted to one side. The shift of the center of the hysteresis loop from the origin is defined as the magnitude of the exchange field (H_{ex}). Furthermore, Co-CoO particles displayed unidirectional, rather than uniaxial, anisotropy[12] which result in a $\sin 2\theta$ function in the torque curve.

Since the discover of the exchange coupling phenomenon, many researchers studied on it to increase the scientific understanding. The physics is the exchange interaction between the antiferromagnet and ferromagnet at their interface. Since antiferromagnets have a small or no net magnetization, their spin orientation is only weakly influenced by an externally applied magnetic field. Therefore, the interfacial moments of ferromagnet which is coupled with the antiferromagnet are pinned and the reversal of the ferromagnet's moment will have an additional energy barrier to overcome the coupling. Thus, the magnetization curve possesses exchange field.

In most ferromagnet/antiferromagnet bilayers, the Curie temperature of

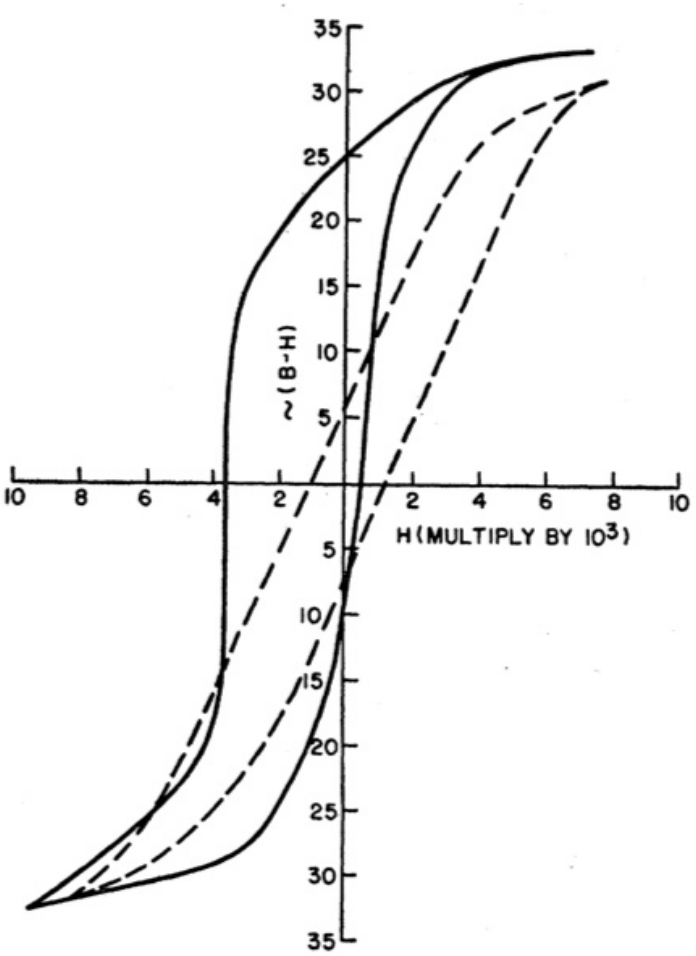

Figure 2.3: Hysteresis loop of the Co-CoO sample cooled in the field and measured at 77K.[11]

the ferromagnet is larger than the Néel temperature (T_N) of the antiferromagnet. This means that the direction of the exchange bias can be set by cooling through T_N in the presence of an applied magnetic field. The moments of the ferromagnet apply an effective field to the antiferromagnet as it orders, setting the anisotropy direction.

Exchange anisotropy has long been poorly understood due to the difficulty of studying the dynamics of domain walls in thin antiferromagnetic films. The first and the simplest approach is the called the ideal interface model suggested by Meiklejohn and Bean.[12] This model use an ideal interface, assuming that the interface is ideal atomically smooth and is perfectly uncompensated in antiferromagnet layer (as shown in figure 2.4). Another simplifying assumption is

that the exchange coupling is much weaker across the interface than in either ferromagnetic or antiferromagnetic layer. This model, the switching field of the ferromagnetic layer coupled with antiferromagnetic layer is determined by the Zeeman energy, magnetocrystalline anisotropy (K_u), and exchange anisotropy (K_e) energies. The energy per unit area can be expressed as fellow:

$$E = -HM_s \cos(\theta - \varphi) + K_u \sin^2\theta - (K_s/t_F)\cos\theta \tag{2.6}$$

Where M_s is the saturation magnetization, t_F is the thickness thickness of the ferromagnetic layer, θ is the angle between the ferromagnetic magnetization and its easy axis, and φ is the angle between the measuring field and the easy axis.

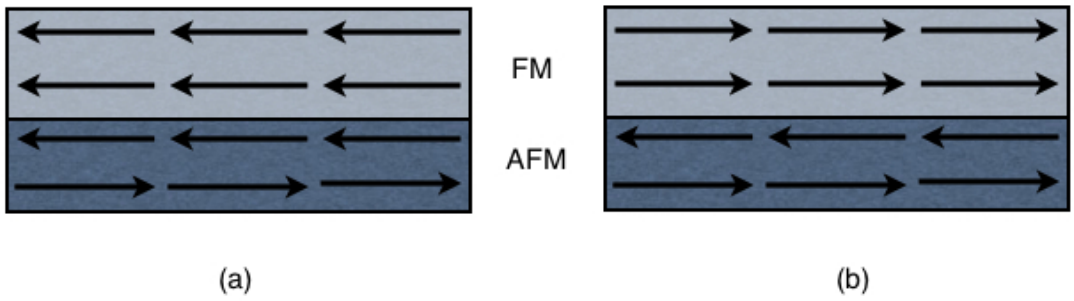

Figure 2.4: Schematic diagrams of spin configurations of the ideal interface. (a) for the $\theta = 0°$ (b) $\theta = 180°$.

For the switch of the ferromagnetic layer form $\theta = 0°$ to $\theta = 180°$ (as shown in fiugure 2.4), from the equation 2.6, the switching field can be expressed as:

$$H_{switching} = 2K_u/M_s + K_e/(M_s t_F) \tag{2.7}$$

In equation 2.7, the first term corresponds to the switching field for the

intrinsic ferromagnet by a coherent rotational process, and the second term corresponds to the exchange field for the ferromagnet coupled to the antiferromagnet. Therefore, the exchange field (H_{ex}) is:

$$H_{ex} = K_e/(M_s t_F) \tag{2.8}$$

To further estimate the magnitude of K_e, considering the exchange energy per atom at the interface (J_{ex}) and the number of atoms at the interface (N), the coupling energy can be expressed as HJ_{ex}. Here, the number of interfacial atoms N is approximately equal to A/a^2, where A is the area of the interface and "a" is the atomic spacing. Therefore, the energy per unit area at the interface (σ) is J_{ex}/a^2. K_e can be approximated by this interfacial exchange energy. Therefore, equation 2.8 becomes:

$$H_{ex} = K_{ex}/(M_s t_F a^2) \tag{2.9}$$

The exchange field is directly proportional to the interfacial energy, but inversely proportional to the magnetization and thickness of ferromagnetic layer. The inverse proportional thickness dependence of exchange is characteristic of a surface effect. This model for exchange anisotropy is simple and describes the observed shifted hysteresis loop and $\sin 2\theta$ function in torque curve. However, the exchange field estimated by the model is two to three orders larger than the experimental value of the exchange field in the NiFe/FeMn system[13].

In order to get closer to the actual experiment of the exchange, the ideal interface model need to be modified. Malozemoff proposed random-field model[13] which consider an rough interface with single monoatomic bump in the compensated simple cubic antiferromagnet interface as shown in figure 2.5. The

monoatomic bump introduces more antiparallel pairs, marked as red crosses, in figure 2.5(b).

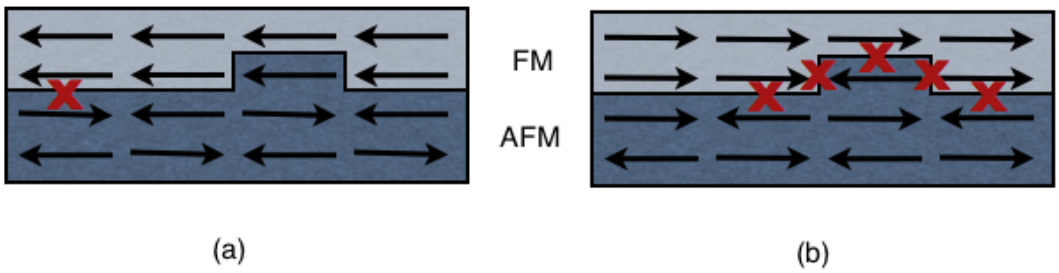

Figure 2.5: Schematic diagrams of possible spin configurations of the random field model.

The local roughness leads to a difference of local interfacial exchange energy which can be expressed as:

$$\sigma_w = zJ_{ex}/a^2 \tag{2.10}$$

where z is the number of order unity, i.e., the correlation number related to the number of antiparallel pairs, J_{ex} is the interfacial exchange-coupling constant, and "a" is the atomic spacing. This model argues that a net average non-zero interfacial energy will exist, particularly when the average is taken over a small number of sites. The average interfacial energy an area of L^2 will decrease as $\sigma_w/\sqrt{N}$, where N, which is the number of sites projected onto the interface plane, equals to (L^2/a^2). Given a random field provided by the interface roughness and a single domain ferromagnet, it is energetically favorable for the antiferromagnet to break up into magnetic domains with domain walls perpendicular to the interface.

Although expansion of the domain size (L) would lower the random field

energy, in-plane uniaxial anisotropy energy (K_{AF}) in the antiferromagnetic layer will limit the domain size. The anisotropy energy confines the domain wall width to $\pi\sqrt{A_{AF}/K_{AF}}$ and creates an additional surface energy term $4\sqrt{A_{AF}/K_{AF}}$ for the domain wall (surface tension in bubble domain), where the A_{AF} is the exchange stiffness which is approximate to J/a. The balance between exchange and anisotropy energy is attained when $L \approx \pi\sqrt{A_{AF}/K_{AF}}$. Hanse, the average interfacial exchange energy becomes:

$$\sigma_w = \frac{4zJ_{ex}}{\pi aL} \tag{2.11}$$

Accordingly, the exchange field due to the interfacial random-field energy density is:

$$H_{ex} = \frac{\sigma_w}{2M_s t_F} = \frac{2z\sqrt{A_{AF}K_{AF}}}{\pi^2 M_s t_F} \tag{2.12}$$

The factor of $\sqrt{A_{AF}K_{AF}}$ reduces exchange field predicted by the ideal interface model to the levels observed in experiments of the NiFe/FeMn system. In this model, the size of the antiferromagnetic domain should be on the same order as the size of domain walls, this implies that most of the interface area actually consists of domain walls. However, this model does not consider the effects of antiferromagnetic domain walls on the exchange field.

In order to explain the discrepancy between the exchange field value predicted by the ideal interface model, Mauri et al. proposed the antiferromagnet domain wall model[14]. This model proposed the formation of a planar domain wall as the reverse of the ferromagnetic layer. The model is illustrated in figure 2.6. The infinitely thick antiferromagnet is assumed to have a uniaxial anisotropy in the z direction. The ferromagnet thickness t is chosen to be much

smaller than the thickness of a domain wall in the ferromagnet. Hence one can assume that the spins in the ferromagnet all include the same polar angles β with the z axis.

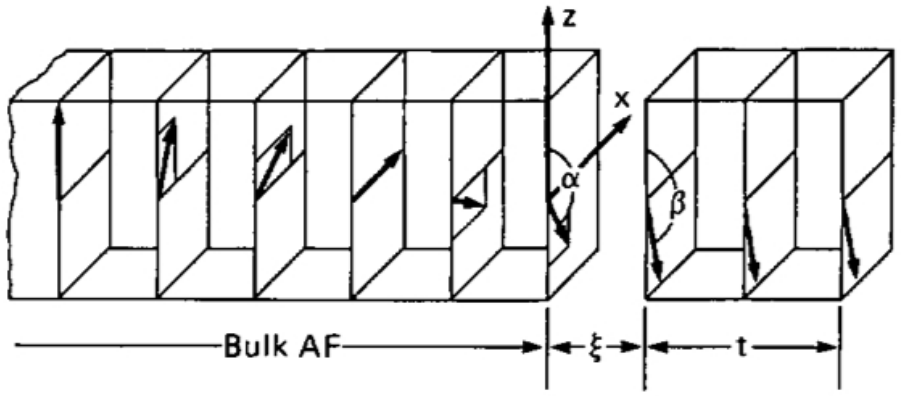

Figure 2.6: Magnetic model for the interface of a thin ferromagnetic film on a thick antiferromagnetic substrate. The uniaxial anisotropy of the antiferromagnet is along the z axis. An external magnetic field is applied opposite to z and the exchange coupling across the interface with thickness ξ positive.[14]

The energy required per unit area of this domain wall is $2\sqrt{A_{AF}K_{AF}}$. The ferromagnet reverses when the Zeeman energy of the ferromagnet is greater than the energy required to form a domain wall in the antiferromagnet. Thus, at the critical point when the ferromagnet start to reverse, these two energy equal to each other which gives $H_{ex}M_F t_F = 2\sqrt{A_{AF}K_{AF}}$. Therefore, the exchange field is:

$$H_{ex} = \frac{2\sqrt{A_{AF}K_{AF}}}{M_s t_F} \tag{2.13}$$

In this model, the exchange energy is not concentrated across a single atomic interface but spreads out over a domain wall of width ($\sqrt{A_{AF}K_{AF}}$). This leads to reduction of H_{ex} by a factor of $\sqrt{A_{AF}K_{AF}}$, which is the same reduction as that of the random field model. However, this model fails to explain the origin of the exchange bias at compensated antiferromagnet surface and the persistence of

exchange anisotropy without diminution of exchange field with antiferromagnet thickness of 25 Å, which is an order of magnitude smaller than the characteristic domain wall width. Nevertheless, this model purpose an important idea that the formation of domain wall in the antiferromagnetic layer is a key issue for the exchange field.

In order to deal with the exchange field in compensated antiferromagnet surface, Koon[15] use micromagnetic calculations based on Heisenberg model to solve the problem. This model assumes a simple body centered tetragonal magnetic structure with exchange interactions along the body diagonals. For the antiferromagnet this leads to the simplest type of antiferromagnetic order in which spins on the two sublattices are oppositely directed and only interact with spins on the other sublattice, as indicated in figure 2.7 (a). Therefore, this structure can be oriented to have a fully uncompensated interfacial spin plane (100) or a fully compensated interfacial spin plane (110). Assuming there is an uniaxial anisotropy in the antiferromagnet crystal along the [001] direction, and no intrinsic anisotropy in the ferromagnet layer.

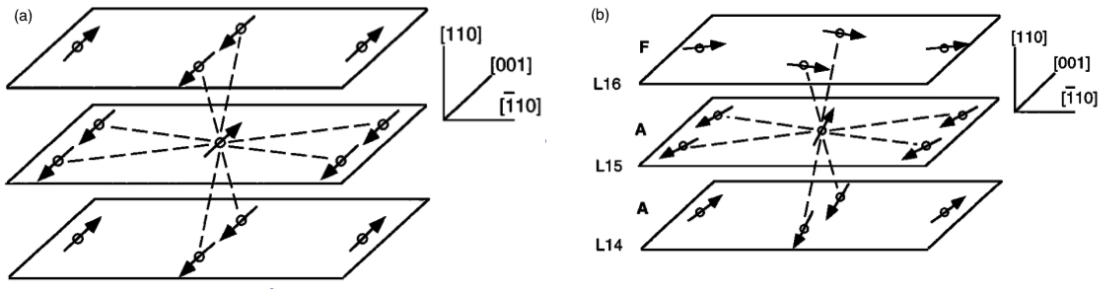

Figure 2.7: (a) Magnetic structure for only antiferromagnetic interactions. (b) Spin configuration near the interface plane with lowest energy orientation. The interfacial AFM plane (L15) is fully compensated, and the interfacial FM plane (L16) is oriented perpendicular. Exchange bonds are shown by the dashed lines.[15]

Two different cases of the AFM interfacial spin plane were applied in this model: (1) a fully compensated interface and (2) a fully uncompensated inter-

face. For both cases, the interfacial energy density as a function of the angle (θ) between the ferromagnetic spins and the Néel axis of the antiferromagnetic spins was calculated. The fully uncompensated interface gives the expected results of collinear coupling, a minimum at $\theta = 0°$. Surprisingly, the fully compensated interface gives the result of a minimum at $\theta \sim 90°$, indicating that the interfacial coupling prefers to the perpendicular coupling. In fact, in the calculation the spins in the antiferromagnet interface exhibit canting. The minimum energy is achieved with the antiferromagnet spins adopting a relatively small canting angle ($\theta < 10°$) relative to the Néel axis, as shown in figure 2.7 (b). The physical picture emerging from this model is that exchange bias results from the formation of a mainly antiferromagnetic parallel domain wall as a reverse field rotates moments of ferromagnet away from the field cooled direction. The domain wall is made possible by strong exchange coupling and pinning of the antiferromagnet by anisotropy.

One year after Koon publish his study, Schulthess and Butler publish their calculation using Koon's spin configuration[16,17]. Different form Koon's work, they use classical micromagnetic approach with Landau-Lifshitz equation of motion and the Gilbert-Kelley form for the damping term. The calculation result shows that contrary to Koon's expectation, spin-flop coupling does not lead to the formation of a domain wall during magnetization reversal but rather introduces a large uniaxial anisotropy. In other words, spin-flop coupling between ferromagnet and antiferromagnet films gives rise to a uniaxial rather than a unidirectional anisotropy. A necessary consequence is that additional mechanisms, such as those induced by interfacial defects, are required to shift the magnetization curve for exchange bias. The asymmetry in the energy minima results in the observation of the exchange field. Therefore, the exchange coupling does not necessary exhibit in the form of exchange field. It can result in

the enhancement of the uniaxial anisotropy or the coercivity.

Another model which is a microscopic model, was purposed in 2001 by Nowak et al.[18,19] This model, called domain state model, introduced a dilutions of nonmagnetic defect in the antiferromagnet. In a result, the exchange field, which are developed during the field-cooling process, arises from the formation of domain states in the antiferromagnet and carry an irreversible magnetization. It is very important to note that the domain state is a metastable state which develops and becomes frozen during cooling. During the field-cooling process, the antiferromagnet which contact with the saturated ferromagnet exposed to an external magnetic field. Figure 2.8 illustrate the spin configuration of the domain state model. The black dots denote nonmagnetic ions or vacancies and the solid line surrounds a domain in which the magnetization is reversed with respect to the background magnetization outside this domain. The number of uncompensated spins of the domain is three and the number of broken bonds at the domain boundary is five. If the sample is field-cooled, the system usually develops metastable domains. The reason for this metastability is a strong pinning which hinders domain wall motion. These pinning effects are due to the dilution as well as to the fact that a rough domain wall also carries magnetization which couples to the external field and hinders domain wall motion.

The geometry of the model is sketched in figure 2.9. During cooling the ferromagnet is initially magnetized along the easy z axis resulting in a nearly constant exchange field for the antiferromagnet monolayer at the interface. The coupling between the ferromagnet and antiferromagnet is shown by the solid line. A net surplus magnetization exists at the interface when the magnetization is averaged over a set number of domains. That is the reason for the exchange

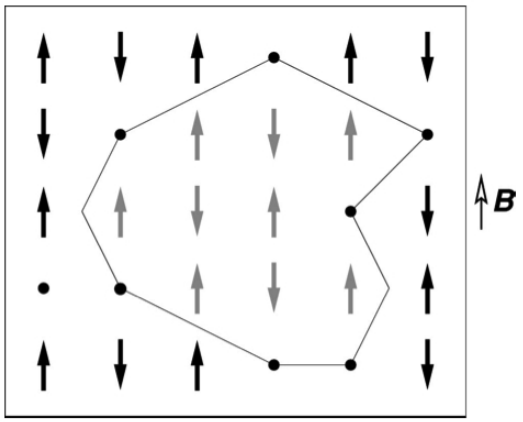

Figure 2.8: Schematic illustration of the domain spin structure.[19]

bias in this model. In this model, domain formation is crucial for the existence of exchange bias. Without domain formation there would be no exchange bias for compensated interfaces and a much too high exchange bias field for uncompensated interfaces. Defects in the antiferromagnet favor domain formation and thus make the distinction between compensated and uncompensated interfaces to a large extent obsolete.

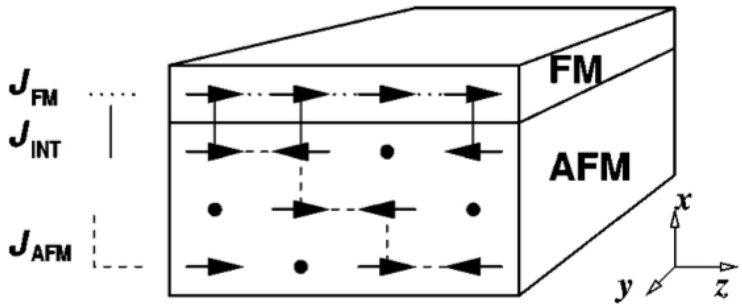

Figure 2.9: Sketch of the model with one ferromagnet layer and three diluted antiferromagnet layers. The dots mark defects.[19]

To overcame the theoretical difficulties in explaining interconnection between the exchange bias and coercivity, Radu et al. purposed the spin glass model[20,21]. This model considered a magnetic state of the interface between ferromagnet and antiferromagnet layer which is magnetically disordered behaving similar to a spin glass system. Assuming the antiferromagnet layer contain

two types of antiferromagnetic states (shown in figure 2.10): frozen-in antiferromagnet spins and rotatable antiferromagnet spins. This interfacial frustrated region of the antiferromagnet is the reason of the increased coercivity. Since the interface between the ferromagnet and antiferromagnet layer is never perfect. This may lead to the formation of a transition region from the pure antiferromagnet state to a pure ferromagnet state. Therefore, it is reasonable to assume that some of the interfacial spins rotate almost in phase with the ferromagnet spins.

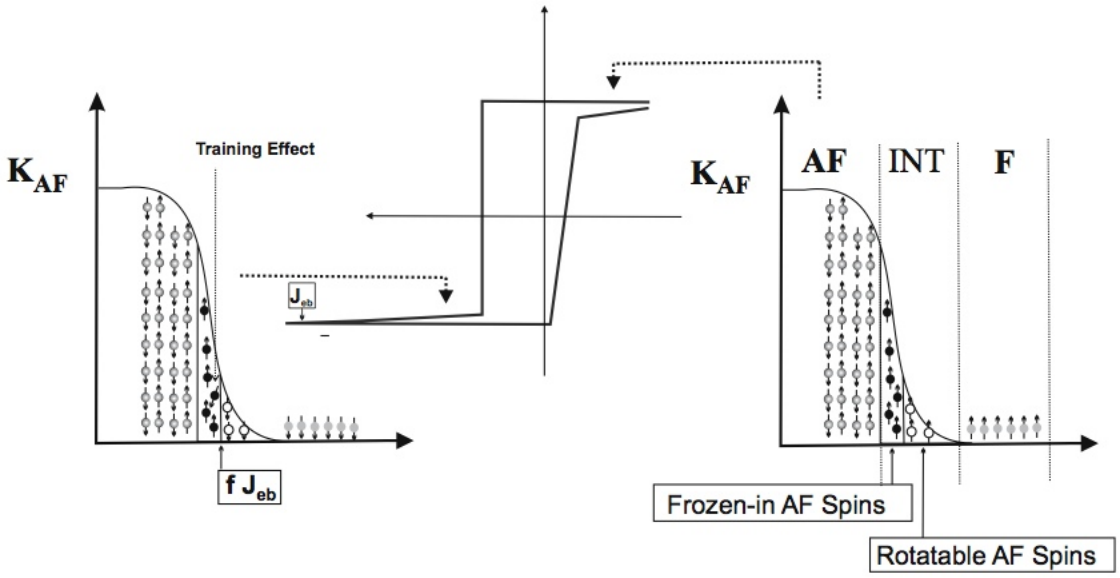

Figure 2.10: Schematic view of the spin glass model.[22]

By those assumptions, revising the ideal interface model, the energy per becomes:

$$\begin{aligned} E = &- HM_s\cos(\theta-\varphi) + K_u\sin^2\theta \\ &+ K_{AF}t_{AF}\sin^2\alpha + K_{SG}^{eff}\sin^2(\varphi-\gamma) - J_{ex}^{eff}\cos(\varphi-\alpha) \end{aligned} \tag{2.14}$$

where, K_{SG}^{eff} is effective uniaxial spin glass anisotropy related to the frustrated antiferromagnet spins at the interface, J_{ex}^{eff} is the effective interfacial exchange energy, and γ is the average angle of the effective spin glass anisotropy.

K_{AF} is the anisotropy constant of antiferromagnet layer. Notice that the Zeeman energies of the ferromagnetic-like antiferromagnet interfacial spins are neglected in this model since they are usually much smaller compared to Zeeman energy of the ferromagnet layer.

Assuming the interface of strong antiferromagnet and ferromagnet layer has a degree of disorder, hanse, the effective anisotropy and the effective interfacial exchange energy can be expressed as:

$$K_{eff} = (1 - f)J_{ex} \tag{2.15}$$
$$J_{ex}^{eff} = f J_{ex}$$

where J_{ex} is the total exchange energy and f is a conversion factor describing the fractional order of the interface. $f = 1$ would represent a perfect interface and $f = 0$ means complete disorder. The exchange field is:

$$h_{ex} = \frac{H_{ex}}{\frac{J_{ex}^{eff}}{M_s}} = \frac{H_{ex}}{f H_{ex}^{\infty}} \tag{2.16}$$

where the H_{ex} is the absolute value of the exchange bias in the spin glass model and the denominator term $\frac{J_{ex}^{eff}}{M_s}$ is the exchange bias field within the ideal interface model. This model successfully describe the azimuthal dependence of the coercivity and exchange bias field and explain the enhance coercivity. Therefore, we can deduce that better control over the exchange bias of magnetic heterostructures could be achieved by controlling the degree of spin disorder and the thickness of the interfacial layer.

2.3 Reduce the ordering temperature of FePt

It is necessary to use a high temperature treatment such as substrate heating during the deposition or post-annealing for FePt in order to obtain the $L1_0$ ordering phase. The high temperature process, however, often induces grain growth which is detrimental for high-density recording.

2.3.1 Ion irradiation

People found that by ion irradiation, ordered FePt thin films can be fabricated without post-annealing processes[23–25]. It was found that He-ion irradiation introduces three major effects. First, microscopic energy would transfer from incident ions to FePt atoms. Second, it generates excess point defects in FePt films, and third, it has the effect of direct beam heating. Due to those effects, the ordering can be achieved at low nominal surface temperature. Moreover, the ion irradiation with beam heating can be potentially used for magnetic patterning[26].

2.3.2 Adding the third element

Several studies reduce the ordering temperature by adding a third element into FePt. It was reported that adding Cu into FePt results in the increase of a driving force of the disorder-order transformation[27]. This is because the Fe atoms of FePt would be substituted by Cu, therefore enhance the diffusivity of the this alloy. For the annealing temperature below 600°C, the FePtCu trinary alloy possesses larger coercivity than FePt binary alloy in the same annealing condition.

Adding Zr into FePt also can reduce the required ordering temperature[28]. In that experiment, the 70nm $(Fe_{59}Pt_{41})Zr_3$ was deposited onto glass substrate and annealed under 500°C for 10 minutes. The coercivity reached 7.3 KOe. It may be that the point defects and lattice strain introduced by Zr-doping increased the nucleation rate of the ordered phase. However, the ordered $L1_0$ phase was turn into a disordered phase after excessive annealing due to the formation of Pt_3Zr phase, which reduces the effective Pt content in the ordered phase.

2.3.3 Forming gas annealing

In 1995, people already used forming gas (5% H_2 mixed with Ar)in the FePt annealing process to prevent the oxidization of FePt[29]. Few years later, researchers notice that the hydrogen can enhance the FePt ordered phase transformation. The ordering temperature of FePt is reduced to 275°C after forming gas annealing[30]. It was found that the coercivity increased with the amount of hydrogen atoms dissolved in the FePt lattices.Therefore, hydrogen atoms may occupy the interstitial sites of FePt, inducing a local strain or an agitation which increases the rate of diffusion of Fe and Pt atoms.

2.3.4 The underlayer effect

In addition to adding the third element, using suitable underlayers can also reduce the ordering temperature and improve the coercivity. The Ti underlayer was found to improve the ordering of FePt[31]. It was speculated that Ti underlayer induce large amounts of dislocations and stacking faults in the FePt film which promote the ordering of the FePt. During the ordering processes,

the a-axis of FePt lattice expands. Therefore, it is believed that introducing a stress on the FePt film is a way to reduce the ordering temperature. The Ag underlayer was reported to be a good underlayer for epitaxial growth of FePt[32,33]. The Si/Ag/FePt epitaxial system was fabricated under 300°C. The lattice constant of Ag is larger than that of FePt, therefore, can assist the a-axis of FePt lattice to expand and thus improve the ordering and promote the perpendicular anisotropy of FePt. J. P. Wang et al successfully grew ordered FePt (002) texture film on the CrRu underlayer[34,35]. By changing the Ru percentage, the lattice constant of the CrRu underlayer can be controlled. Therefore, the increase of the Cr lattice constant with the Ru percentage in a Cr underlayer increases the lattice mismatch between the Cr(002) and the FePt (001) planes. As the misfit increase, the strain between FePt (001)[100]/Cr(002)[110] become larger. As a result, the strain enhanced the FCT phase formation. As shown in figure 2.11, with the Ru content in the Cr underlayer, the the lattice misfit increases linearly. The misfit reaches maximum at 11.6 at. % of Ru then drops. On the other hand, the out-of- plane coercivity increases with the Ru percentage and reaches maximum at 9.0 at. % Ru, then decreases as the Ru content further increases. These results indicate that as the Ru percentage exceed 9.0 at. % induce intolerably lattice mismatch of the lattice between FePt and CrRu underlayer, hence it may induce higher density of defects and release the stress which built by the lattice mismatch. It is generally believed that the orientation of the c axis of FePt is mostly related to the stress state.

2.3.5 The stress effect

People believe that the stress is closely related to the ordering process of the FePt. In our previous work, we have proved that the formation of the Cu_3Si

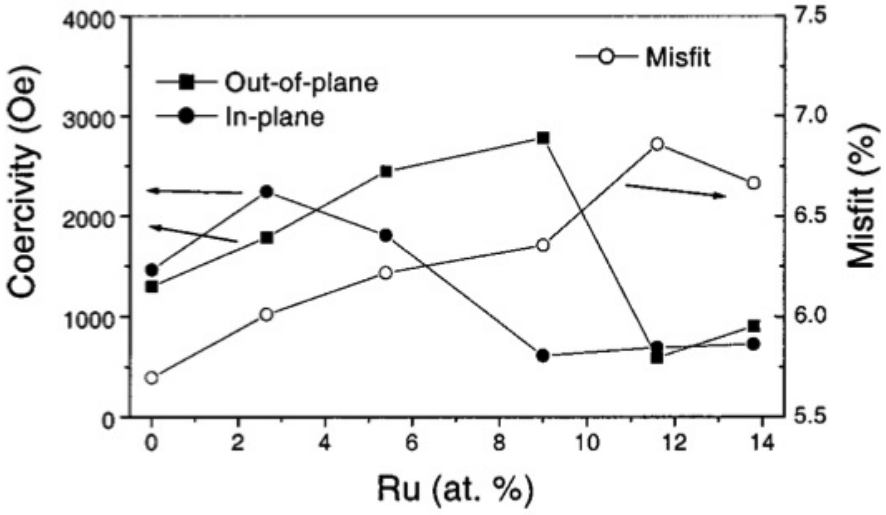

Figure 2.11: The variation of the coercivities with substrate temperature for $Cr_{91}Ru_9$/Pt/FePt samples.[34]

induce an in-plane tensile stress which accelerated the formation of the ordered FePt phase[36]. Unlike the static stress induced by the lattice mismatch between films and underlayers, the dynamic stress is relaxed after the formation of Cu_3Si is completed; therefore, the low-temperature ordering of FePt mainly occurs simultaneously with the evolution of dynamic stress during the formation of Cu_3Si.

2.4 Nanocomposite

Recording media traditionally have a single magnetic storage layer and consist of weakly coupled magnetic grains. The fine microstructure allows storing transitions at high linear densities, with the ultimate density limited by the grain size[37]. As illustrated in figure 2.12, the bit transitions follow the grain boundaries, which provide strong pinning sites for the magnetic transitions. Hence, researchers try to fabricate nanocomposite FePt recording films in order to achieve high recording density.

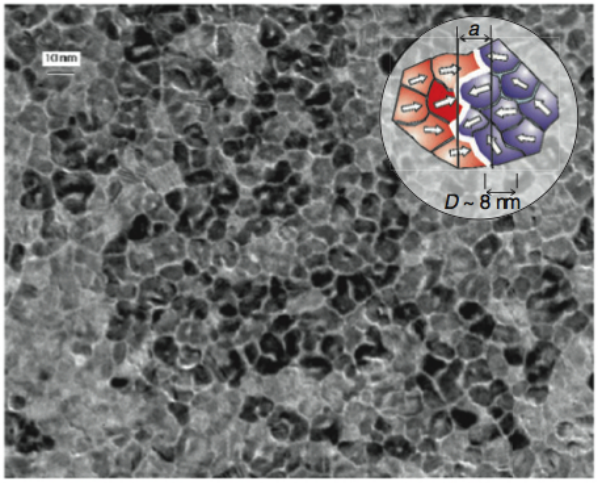

Figure 2.12: TEM image of recording CoCrPtB media. The inset schematically shows a magnetic transition meandering between the grains.[37]

FePt:C perpendicular nanocomposite film has been successfully fabricated and has been widely studied in recent years[38–41]. FePt:C nanocomposite thin films with strong perpendicular magnetic anisotropy can be fabricated by co-sputtering directly on a MgO(100) substrate at elevated substrate temperatures. Under the appropriate C doping, these films consist of $L1_0$ FePt particles embedded in the C matrix with c axes of the grains oriented along the film's normal direction. The grain size and the size distribution can be controlled by the doping of the C. The grain size is 5.2nm with 25% C doping and with further reduction to 4nm with C 50%. However, the x-ray diffraction shows that the intensity of the $L1_0$ ordering peaks are predominant initially, then reduced with increasing C doping. Subsequently, the ratio of the FePt (200)/(002) peaks increases with increasing C amount and merge into a single peak for 50% C doping, suggesting that the amount of ordered and disordered materials in FePt system could be controlled by C doping[38]. The FePt:C nanocomposite film had already successfully integrated with soft underlayer[39,41] with the (100) textured MgO intermediate layer and the FePt:C nanogranular films consisting of well isolated FePt particles of about 5nm with a size distribution of 1.4nm.

The FePt:C films show excellent nanostructure and magnetic properties and therefore are good media for extremely high density perpendicular recording.

FePt:B_2O_3 nanocomposite thin films are also potential media for high density perpendicular recording. In 2000, D. J. Sellmyer et al. deposited FePt/B_2O_3 multilayers onto glass substrate by sputtering and post annealed at 550°C. After annealing, nanostructured FePt:B_2O_3 films consisting of FePt grains with $L1_0$ structure, embedded in a glassy B_2O_3 matrix were obtained[42]. By increasing the thickness of the B_2O_3 in the multilayer, the poly crystal FePt film becomes a textural film. The intensity of the (111) diffraction peaks decreases as the B_2O_3 layer thickness increases in the FePt/B_2O_3 multilayers. As the B_2O_3 layer thickness increases to 12Å and above, the (111) peak disappears and becomes mainly consisting of (001) and (002) peaks, which implies that the c axes of the grains are aligned along the film's normal direction.

Later in 2008, K. Takahashi et al. explained the mechanism of the c-axis orientation in FePt:B_2O_3 nanocomposite thin films[43]. They found that there are three characteristic features when FePt:B_2O_3 c-axis orientation occurs in the thin films: the marked crystallographic orientation occurs during the cooling process, the axial ratio c/a observed experimentally tends to be considerably lower than the equilibrium value, and the degree of c-axis orientation is lowered for a relatively thick film, that is, the plane-stress state plays a key role making the c-axis perpendicular to the film surface. Figure 2.13 shows the mechanism of the c-axis orientation upon the cooling process. When the thin films are heated up to 550°C, B_2O_3 layers become soft and fluidic because the annealing temperature is higher than the melting temperature of B_2O_3. Upon subsequent cooling, B_2O_3 becomes solidified or highly viscoelastic state. Due to the difference in the thermal shrinking between the two substances, it is considered

that in-plane tensile stresses are yielded (Figure 2.13 (b)). When the ordering of FePt occurs under such tensile stresses, the macroscopic shape of the FePt nanoparticles is changed, accompanied by the occurrence of the tetragonal distortion (Figure 2.13 (c)), the FePt are also rotated to the (001) direction in terms of minimization of the total mechanical energy (Figure 2.13 (d)). Therefore, the FePt particles with the c-axis parallel to the normal direction of the film surface are the most stabilized.

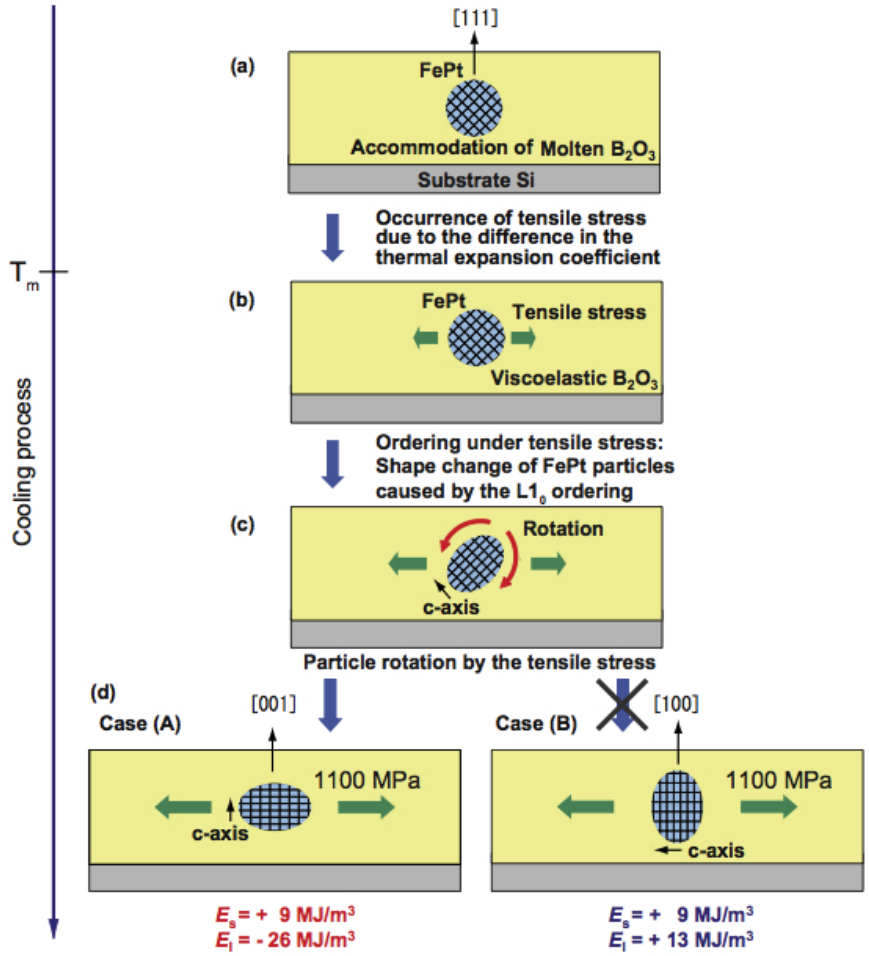

Figure 2.13: Schematic illustration of the mechanism of the c-axis orientation upon cooling process. (a) Accommodation of molten B_2O_3 to FePt nanoparticles. (b) Occurrence of tensile stress due to the thermal shrinking difference between FePt and B_2O_3. (c) Macroscopic shape change of FePt particles due to the tetragonal distortion and rotation of particles caused by ordering under the tensile stress. (d) Preferable rotation of the ordered FePt nanoparticle.[43]

2.5 First order reversal curves

First order reversal curves (FORC) diagram provides a detailed characterization of the hysteretic response of a magnetic system to an applied field[44]. A FORC diagram is generated from a class of minor hysteresis loops. The measurement of a FORC, as shown in figure 2.14, begins with the saturation of the sample by a large positive applied field. Than, the applied field is lowered to a reversal field H_r. The FORC consists of the measurement of the magnetization of the field as it increases from H_r back up to saturation. The magnetization at the applied field H on the FORC with reversal field H_r is denoted by $M(H, H_r)$, where $H \geq H_r$. A FORC distribution is defined as:

$$\rho(H, H_r) \equiv -\frac{1}{2}\frac{\partial^2 M(H, H_r)}{\partial H_r \partial H} \tag{2.17}$$

When a FORC distribution is plotted, it is convenient to change the coordinates system to one based on local coercivity H_c and bias field H_b, where H_c and H_b is defined as:

$$\begin{aligned} H_c &\equiv \frac{H - H_r}{2} \\ H_b &\equiv \frac{H + H_r}{2} \end{aligned} \tag{2.18}$$

This FORC distribution resembles the Preisach model[45].

The Preisach model define a simple mathematical construction, which is referred as a hysteron. As shown in figure 2.15, the hysteron denoted by $\gamma_{\alpha\beta}$ equals 1 for large values of H; it switches to -1 when H is below H_α, and it remains at -1 until H passes H_β. When the second derivative in equation 2.17 is taken for the hysteresis behavior of $\gamma_{\alpha\beta}$, the resulting $\rho(H, H_r)$ will have a

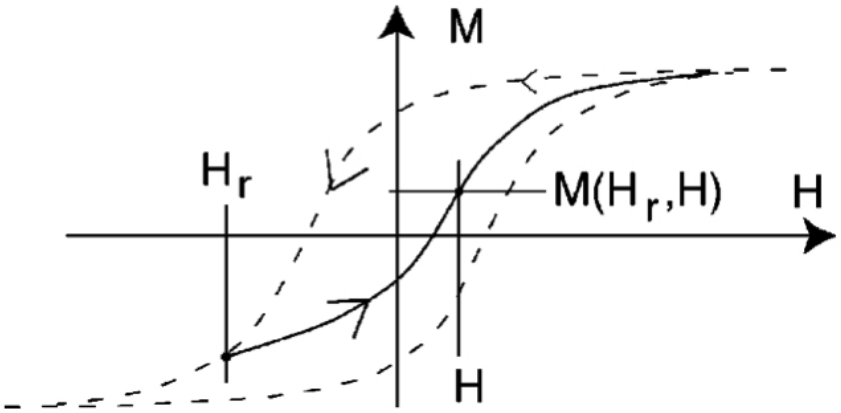

Figure 2.14: The measurement of a FORC begins with the saturation of the sample by a large positive field. The applied field is lowered to a reversal field H_r. A FORC is the magnetization curve that results when the field is increased back to saturation. The magnetization at the applied field H on a FORC with reversal field H_r is denoted by $M(H, H_r)$.[46]

peak at $H = H_\alpha$ and $H_r = H_\beta$, and will equal zero elsewhere. Hence, the FORC distribution ρ relates to the statistical distribution of mathematical hysterons.

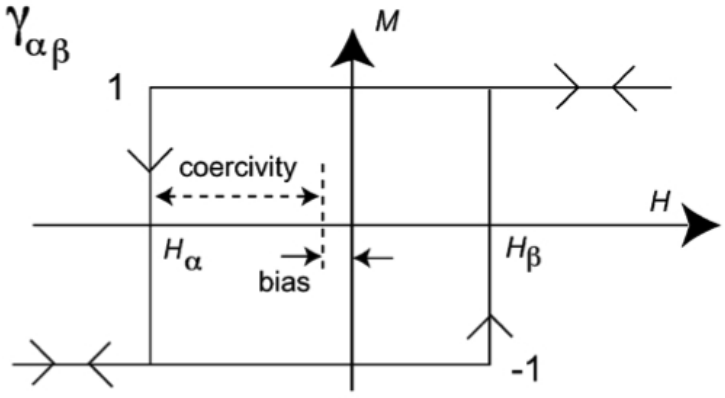

Figure 2.15: The hysteron $\gamma_{\alpha\beta}$ equals 1 for large values of H, switches to -1 when H falls below H_α and remains at -1 until H rises above H_β. The half-width of the hysteron is its coercivity, and the horizontal offset of its centre is its bias.[47]

The Preisach model of hysteresis was first suggested as a model for interacting single domain particles. In this model, each hysteron represents an individual particle in the assemblage. The coercivity of a hysteron corresponds to the coercivity of a single domain particle if it were magnetically isolated from

other particles. The bias of a hysteron corresponds to a fixed interaction field which represents the magnetostatic interaction of an individual particle with the surrounding assemblage of particles. The Preisach distribution therefore corresponds to the distribution of particle coercivities and interaction fields[47].

A FORC distribution is simply a well-defined transform of the set of first order reversal curves. On the contrary, Preisach distribution assumes a symmetry condition: if an applied field history H(t) gives a magnetization M(t), then the opposite applied field history -H(t) must give the opposite magnetization -M(t). This means that the Preisach distribution is symmetric about the $H_b = 0$ axis. However, experimental FORC distributions are not, in general, symmetric about the $H_b = 0$ axis. A FORC distribution, compared to Preisach model, is not part of a theoretical model. Therefore, FORC diagrams can be used to obtain a more detailed understanding of magnetic interactions.

Chapter 3

Experimental techniques

3.1 Sample fabrication

The (111) texture and (001) epitaxial FePt thin films were deposited by the magnetron sputtering system. The sputtering system has six sputtering sources and is composed of two main parts. One is the growth chamber, and the other is the loading chamber, as illustrated in figure 3.1. The pumping systems contain two mechanical pumps, and two turbo pumps. The base pressure of the growth chamber is 2×10^{-7} Torr, which provides a good control of the thin film deposition and the low impurity contamination. The working pressure used for the deposition process is 3 mTorr with the sputtering atmosphere of Ar. All sputtering sources are tilted and targeting the sample holder. There is a heater right under the sample holder. This system is designed for high temperature deposition. Therefore, is it suitable for the epitaxial growth.

Figure 3.1: Picture of the magnetron sputtering system.

3.2 Structure characterization

3.2.1 X-ray diffractometer

The essential feature of the x-ray diffractometer is illustrated in figure 3.2. The rotating axes of the specimen and the detector are defined as θ and 2θ axes with respect to the incident beam, respectively. The detector can rotate about the specimen and set at any desired angular position. The crystal is usually cut or cleaved so that a particular set of reflecting planes of known spacing is parallel to its surface, as suggested by the drawing. In practice, the specimen is rotated with a angle of θ to the incident beam, and the detector is set at the corresponding angle of 2θ, as illustrated in figure 3.2. The intensity of the diffracted beam is then measured by the detector with a continuous angular scan. When the out-of-plane crystallographic planes fulfill the Bragg's law ($2d \sin\theta = n\lambda$) at certain angle of θ, and the structure factor of the crystallographic plane in the specimen for the diffraction process is not zero, the constructive interference

occurs, resulting a detectable diffraction peak.

The directions in which a beam of given wavelength is diffracted by a given set of lattice planes are determined by the crystal system to which the crystal belongs and its lattice parameters. This is an important point and so is its converse: all we can possibly determine about an unknown crystal by measurements of the directions of diffracted beams are the shape and size of the unit cell. In addition, the intensities of diffracted beams are determined by the positions of atoms within the unit cell.

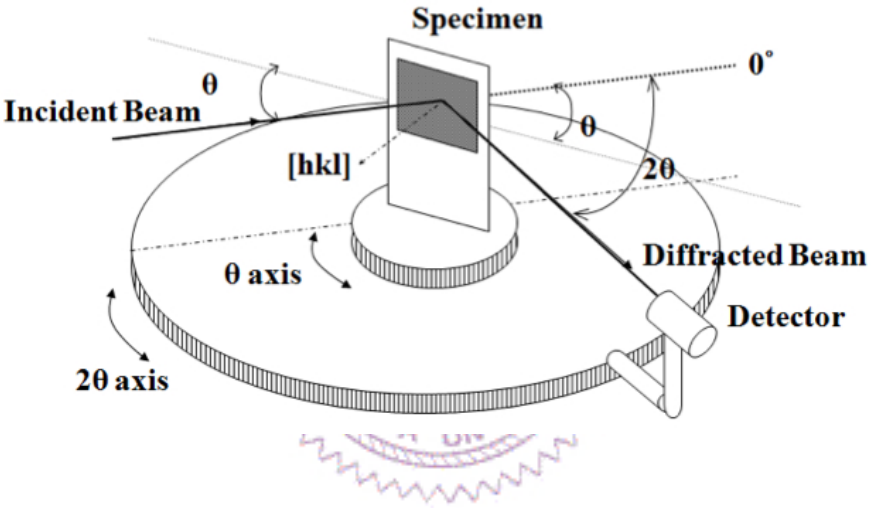

Figure 3.2: The schematic illustration of the x-ray diffractometer.

3.2.2 X-ray ϕ scan

To verify the epitaxial relationships of FePt on MgO subtract, x-ray ϕ scans were performed to investigate diffraction peaks of planes that are not parallel to the film surface. The principle of the in-plane x-ray ϕ scan is schematically illustrated in figure 3.3. If the film is a cubic (001) textured system with random in-plane orientations, all normal directions of equivalent {111} planes are uniformly distributed on the surface of the cone with the angle of 54.74 °from the [001] film normal. On the other hand, if the film is a cubic (001) epitaxial system with a single in-plane orientation, only four <111> normal directions

lie on the surface of the cone due to the four-fold symmetry of {001} planes. Consequently, when we tilt the sample to an off-axis orientation, the diffraction scans by rotating the sample along the film normal direction should enable us to distinguish epitaxial films from textured films.

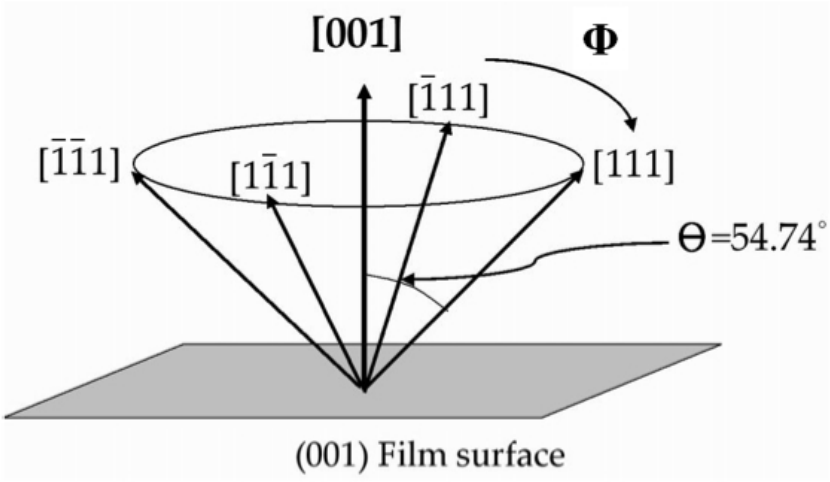

Figure 3.3: The schematic illustration of the x-ray ϕ scan.

3.2.3 Atomic force microscope and magnetic force microscope

The atomic force microscope (AFM), as illustrated in figure 3.4, is a high-resolution scanning probe microscope. The AFM consists of a cantilever with a sharp tip (probe) at its end that is used to scan the specimen surface. The sample is mounted on a piezoelectric tube, that can move the sample in the z direction for maintaining a constant force, and the x and y directions for scanning the sample. Alternatively a 'tripod' configuration of three piezo crystals may be employed, with each responsible for scanning in the x,y and z directions. Typically, the deflection is measured using a laser spot reflected from the top surface of the cantilever into an array of photodiodes. The photo-detectors measure the difference in light intensities between the upper and lower photo-detectors, and then convert it into voltage. Feedback from the photodiode

signal to the software controlled by the computer enables the tip to maintain either a constant force or a constant height above the sample surface. In our experiment, we use tapping mode conditions to analyze our samples. In tapping mode, the cantilever is driven to oscillate up and down at near its resonance frequency by a small piezoelectric element mounted in the AFM tip holder similar to non-contact mode. Due to the interaction of forces acting on the cantilever when the tip comes close to the surface, Van der Waals force, dipole-dipole interaction, electrostatic forces, etc. cause the amplitude of this oscillation to decrease as the tip gets closer to the sample. An electronic servo uses the piezoelectric actuator to control the height of the cantilever above the sample. The servo adjusts the height to maintain a set cantilever oscillation amplitude as the cantilever is scanned over the sample. A tapping AFM image is therefore produced by imaging the force of the intermittent contacts of the tip with the sample surface.

Magnetic force microscope (MFM) is a variety of atomic force microscope, where a sharp magnetized tip scans a magnetic sample; the tip-sample magnetic interactions are detected and used to reconstruct the magnetic structure of the sample surface. Many kinds of magnetic interactions are measured by MFM, including magnetic dipole–dipole interaction. When the tip scans the surface of a sample at close distances (<100 nm), not only magnetic forces are sensed, but also atomic forces. The MFM can be used to image various magnetic structures including domain walls, closure domains, recorded magnetic bits, etc. Furthermore, motion of domain wall can also be studied in an external magnetic field.

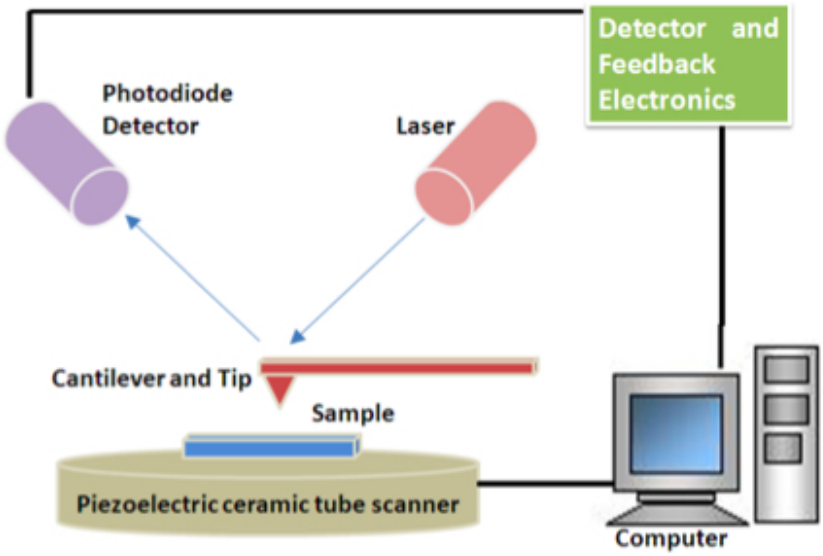

Figure 3.4: The schematic illustration of the atomic force microscope.

3.3 Magnetic characterization

3.3.1 Vibrating sample magnetometer

The principle of the vibrating sample magnetometer is vibrating the sample near the detection coils, as illustrated in figure 3.5, resulting in the variation of magnetic flux and thus the induced electromotive force. The large electromagnet provides a uniform DC field to the magnetic sample. The emanating magnetization is then measured by vibrating the sample to produce a flux change and therefore to induce a voltage in the pickup coils mounted on both sides of the magnet pole pieces. The coil output voltage is combined with the output from the displacement transducer to produce a magnetization signal. As a result, variations in vibration amplitude and frequency are cancelled out. Then, the electromotive-force signal is detected, by a lock-in amplifier, and transmitted along with the applied field signal to a computer to generate a hysteresis loop.

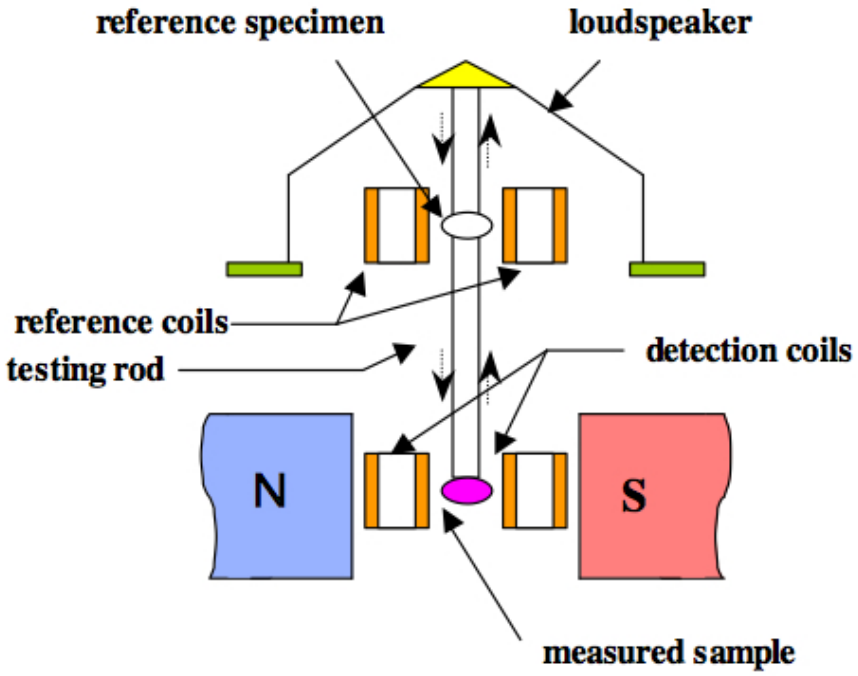

Figure 3.5: Schematic illustrations of the vibrating sample magnetometer.

3.3.2 X-ray magnetic circular dichroism

X-ray magnetic circular dichroism (XMCD) is a difference spectrum of two x-ray absorption spectra (XAS) taken in a magnetic field, one taken with left circularly polarized light, and one with right circularly polarized light. By closely analyzing the difference in the XMCD spectrum, information can be obtained on the magnetic properties of the atom, such as its spin and orbital magnetic moment. In the case of transition metals, typically, L-edge X-ray spectrum was detected, which can best probe the properties of 3d electrons. The origin of magnetic dichroism can be found in the photon-matter interaction process. In X-ray absorption it is not directly due to the interaction between the transverse field B of the photon and the spin of the electrons but rather to the interaction between the spin and the orbit, which couples the spin and real space.

The use of circularly polarized X-rays opens the door for X-ray-based spectroscopy studies of magnetic materials and structure. The basic concept of XMCD spectroscopy is easily understood if we assumed that the d shell has only a spin moment. To measure the difference in the number of d holes with up and down spins, we need to make the X-ray absorption process spin-dependent. Since spin flips are forbidden in electric dipole transitions, spin-up (spin-down) photoelectrons from the p core shell can only be excited into spin-up (spin-down) d hole states. Hence, if one could preferentially generate spin-up photoelectrons in one measurement and the spin-down in another, the difference of the transition intensity in the spectra would simply reflect the difference between up and down holes in the d shell. i.e. the spin moment. This is done by use of right or left circularly polarized photons which transfer their angular momentum to the excited photoelectrons and the difference between the spectra of right- and left-circularly-polarized X-ray is the XMCD spectrum[48].

In this study, XMCD measurements were made at the Dragon beam line at the Synchrotron Radiation Research Center in Taiwan. the XMCD spectra were obtained in a fluorescent light. The samples were introduced in an UHV experimental chamber. The pressure during the measurements was below 1×10^{-9}Torr. We fixed the circularity and the energy of the incident polarized photons and change the applied field on our samples to get the element specific magnetic loops.

3.3.3 Polarized neutron reflectometry

Reflectometry involves measurement of the intensity of a beam of electromagnetic radiation or particle waves reflected by a planar surface and interfaces. The technique is intrinsically sensitive to the difference of the refractive index

across surfaces and interfaces. Polarized neutron reflectometry (PNR) is a tool to investigate the magnetization profile near the surfaces of crystals, thin films and multilayers. By different glancing incident angle, the in-plane average of the scattering density can be obtained at any specified distance along the normal of the surface by counting the number of neutrons elastically and specularly reflected from a flat surface. From this scattering length density profile, the concentration of atoms of a given type at a particular depth can be inferred. If the incident beam is polarized and the resultant polarization of the reflected beam is analyzed, possible magnetic contributions to the scattering density can be determined.

In this study, PNR measurements were conducted using the NG-1 Reflectometer at the National Institute of Standards and Technology (NIST) Center for Neutron Research. An incident monochromatic neutron beam was polarized to be alternately spin up or down relative to H. The non-spin-flip reflectivity (with incident beam spin up or down) and the spin-flip reflectivity (up to down and down to up) were measured as functions of the scattering vector Q.The samples' depth-dependent nuclear scattering length density profiles $\rho_{N(z)}$ (functions of the scattering potential of the constituent nuclei at different depths z beneath the sample surface) and M(z) profiles were determined by model fitting the PNR data, using exact dynamical calculations. Measurements were conducted at room temperature.

Chapter 4

Low-temperature ordering of $L1_0$ FePt by PtMn underlayer

Low-temperature ordering of the high-anisotropy $L1_0$ FePt phase has been extensively studied in recent years. In this chapter, we discuss the effect of PtMn underlayer on the ordering and the coercivity of FePt.

The ordered phase of antiferromagnetic PtMn is also $L1_0$ phase. A typical annealing temperature to achieve the ordered phase of PtMn (250°C)[49] is much lower than an ordering temperature of FePt (500°C), and the c/a ratio of PtMn is 0.92 which is lower than the ratio of FePt (0.96)[50]. The a-axis lattice constants of the ordered PtMn and FePt are 0.40 and 0.387 nm, respectively. The larger lattice constants and lattice deformation during phase transformation of PtMn may promote ordering of FePt at reduced temperatures. Moreover, because of a lower $L1_0$ ordering temperature of PtMn, PtMn is expected to be an ideal underlayer to induce ordering of a $L1_0$ FePt phase at a low temperature. In addition, the exchange coupling between antiferromagnetic (AFM) PtMn and ferromagnetic (FM) FePt may introduce extra anisotropy, and thus may further enhance coercivity of FePt. Therefore, we choose PtMn for the study topic.

4.1 Experiment

FePt films were co-sputtered from elementary targets at room temperature with a structure of Si//SiO_2/Fe 1/Pt 9/PtMn 50/FePt 15-50 (unit: nm). The Fe and Pt underlayers were used to enhance the PtMn and FePt (111) texture. Highly-oriented (111) texture of PtMn and FePt films were obtained in the as-deposited state. For comparison, films with Si//SiO_2/FePt 15-50 (unit: nm) were also prepared. All samples were annealed under vacuum (2×10^{-6} Torr) at 250°C to 300°C for 2hours. In order to study the exchange coupling between PtMn and FePt layers, samples were annealed under an external field of 3000 Oe. The hysteresis loops were measured using a vibrating sample magnetometer (VSM). X-ray diffraction (XRD) θ-2θ scans using the Cu K_α line were performed to identify the structure. Depth profiles of compositions were verified by a secondary ion mass spectrometer (SIMS).

4.2 Results and discussion

Dependence of coercivity on annealing temperature for 50 nm FePt with or without PtMn underlayers is shown in figure 4.1. Field-annealed FePt films grown on PtMn underlayers show much higher coercivity than FePt films alone. Notice that coercivity can reach 1800 Oe just after 250°C annealing and can be increased to 5000 Oe after 275°C annealing. The coercivity of 50 nm FePt on a PtMn underlayer annealed at 325°C is as high as 9700 Oe. PtMn underlayers clearly show the enhanced coercivity at low-temperature annealing.

Figure 4.2 shows XRD results of as-deposited and annealed FePt (50 nm) films with or without PtMn underlayers. Samples were annealed at 300°C for 2 hours. For single layer FePt, there is no major change before and after

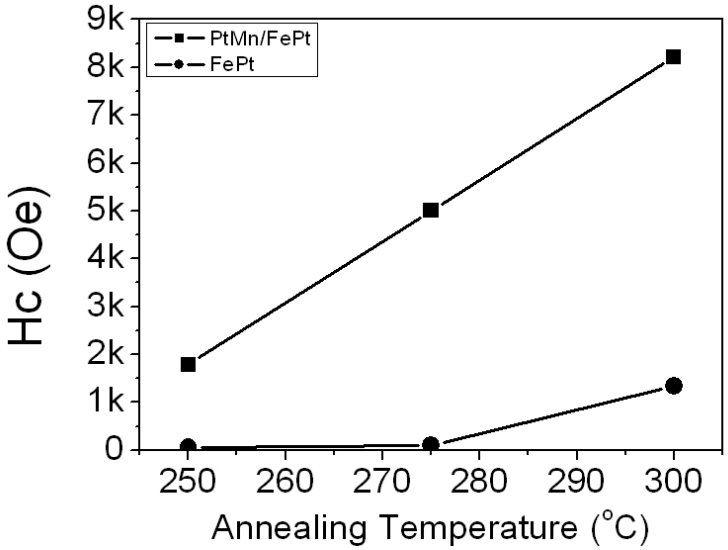

Figure 4.1: Coercivity dependence on annealing temperature for samples PtMn 50 nm/FePt 50 nm and single FePt 50 nm. Samples of PtMn/FePt were field annealed.

annealing, indicating a low degree of ordering. On the contrary, for FePt films grown on PtMn underlayers, both of (111) peaks of FePt and PtMn shift to higher angles after annealing, indicating that phase transformations of FePt and PtMn occur during annealing. This result suggests that ordering of PtMn at a low temperature accelerates ordering of FePt. When annealing temperature reaches the ordering temperature of PtMn, the a axis of PtMn is expanded and the c axis is compressed. These lattice changes of PtMn layers may induce the corresponding changes of disordered FePt lattices, which may promote ordering of FePt at reduced temperatures.

A PtMn underlayer increases coercivity of FePt in two ways. The ordering of PtMn enhances the ordering of FePt; therefore, the coercivity is increased due to a higher degree of ordering, suggested by the peak shift in figure 4.2. Another origin of enhanced coercivity may arise from exchange coupling between PtMn and FePt. This exchange coupling increases the effective anisotropy of FePt. Figure 4.3 shows hysteresis loops of 15nm FePt samples with and without PtMn layer annealed with an in-plane field of 3000 Oe at 250°C for 2 hours. The

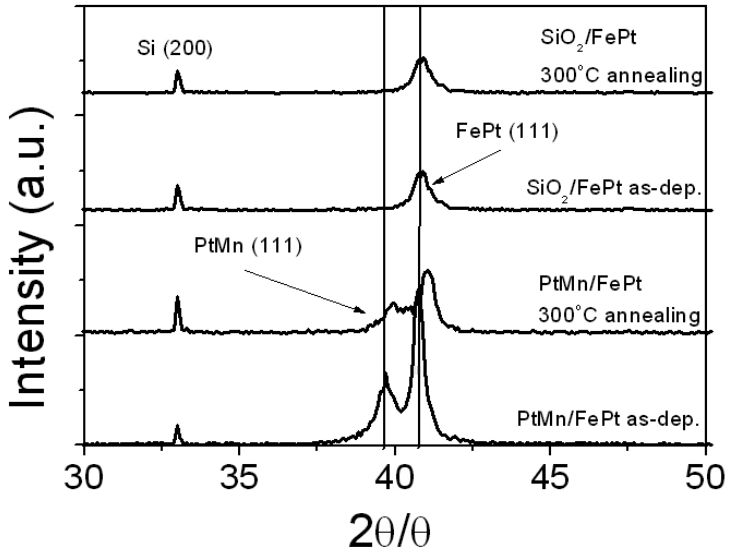

Figure 4.2: XRD results of the as-deposited and annealed FePt (50 nm) films with or without PtMn underlayers. Samples are annealed at 300°C for 2 hours. The lines were used to show the peak shift.

sample with PtMn underlayer shows larger coercivity compared with the sample without PtMn underlayer. Also, the sample with PtMn underlayer shows a clear loop shift of 195 Oe which is due to the exchange coupling between FePt and PtMn.

To investigate the effects of the exchange coupling, the samples with the structure Si//SiO_2/Fe 1 nm/Pt 9 nm/PtMn 50 nm/FePt 10–50 nm were annealed with or without an in-plane field at 325°C for 2 hours. Samples annealed in a field show significantly enhanced coercivity at FePt thickness of 10 and 15 nm, shown in figure 4.4. Exchange fields of 554 and 415 Oe were obtained for 10 and 15 nm FePt, respectively. The differences in coercivity become insignificant for 35 and 50 nm FePt films annealed with or without a field. Low exchange fields (<100 Oe) were observed in both samples. Notice that a huge coercivity of 10500 Oe can be obtained for 35 nm FePt grown on PtMn after 325°C annealing. Since the exchange bias between FM and AFM is an interfacial coupling, an exchange field is reduced with increasing thickness of FePt. At low FePt

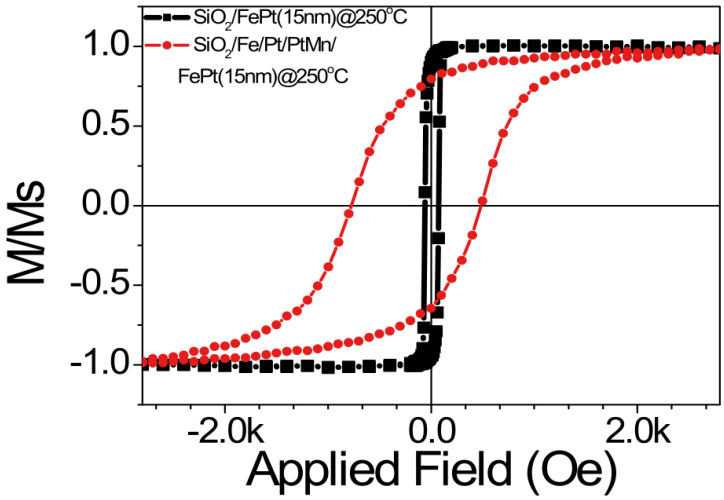

Figure 4.3: Hysteresis loops of samples with structure of Si//SiO_2/Fe 1 nm/Pt 9 nm/PtMn 50 nm/FePt 15 nm and Si//SiO_2/FePt 15 nm. Samples were annealed with an in-plane field of 3000 Oe at 250°C for 2 hours.

thickness, the magnetization of field-annealed FePt films was partially aligned and pinned by the interfacial spins of PtMn. Consequently, the field-annealed samples exhibited much enhanced coercivity. On the other hand, the coercivity of single FePt increases with increasing thickness after the same annealing procedure; therefore, the magnetocrystalline anisotropy becomes dominant and the anisotropy contributed from exchange bias was relatively small at thick FePt films; consequently, field-annealing does not provide prominent effects.

Since the exchange coupling is a short-range coupling, a relatively thick Pt layer (10 nm) was inserted between FePt and PtMn layers to further study the effects of exchange bias on coercivity of FePt. The sample structure is: Si//SiO_2/Fe 1/Pt 9/PtMn 50/Pt 10/FePt 15-50 (unit: nm). Samples were annealed at 300°C for 2 hours under a 3000 Oe external field. Figure 4.5 shows the FePt thickness dependence of coercivity. All samples without the Pt intermediate layer show higher coercivity than those with Pt layers. The Pt intermediate layer eliminates the exchange coupling between PtMn and FePt, resulting in

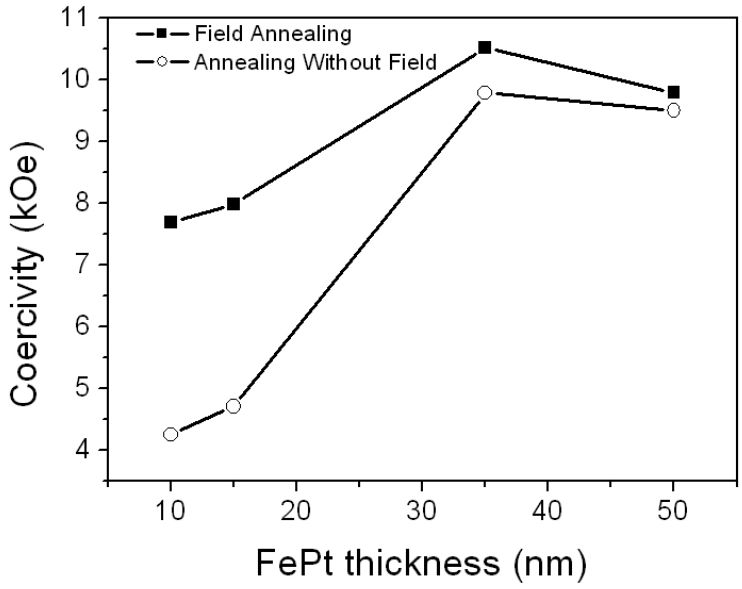

Figure 4.4: Dependence of coercivity on FePt thickness for samples Si//SiO_2/Fe 1 nm/Pt 9 nm/PtMn 50 nm/FePt 10–50 nm. Samples were annealed with or without an in-plane field of 3000 Oe at 325°C for 2 hours.

reduction of FePt coercivity. In addition, the thick Pt layer might partially suppress the effects of PtMn-induced ordering of FePt, because lattice changes of PtMn during its ordering process may not directly affect FePt lattices.

During annealing, Mn diffusion from PtMn underlayers to FePt layers may occur, which might alter coercivity of FePt. The addition of Mn may reduce the anisotropy of FePt thus reduce the coercivity[51,52]. However, the Mn doping in FePt nanoparticles resulted in an enhanced coercivity of FePt[53]. Composition depth profiles were taken using SIMS of the sample Si//SiO_2/Fe 1 nm/Pt 9 nm/PtMn 50 nm/FePt 50 nm annealed at 300°C for 2 hours. The result, shown in figure 4.6, indicates that Mn diffusion occurs only at the interface. Mn diffusion at interface might behave as pinning sites but its effects need to be further investigated. However, figure 4.4 shows that the field- annealed and zero-field-annealed samples indeed exhibit different coercivities at thin FePt thickness. This result implies that Mn diffusion may not be a key factor to determine

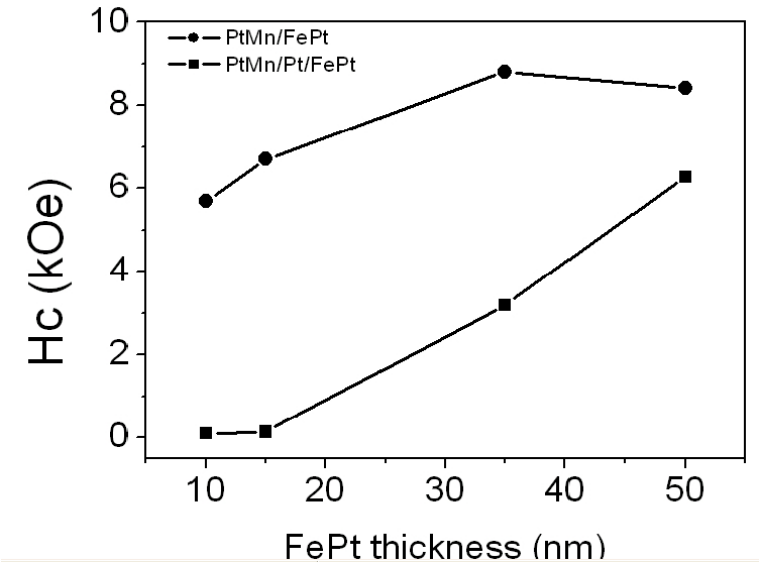

Figure 4.5: Coercivity dependence of FePt thickness for samples Si//SiO_2/Fe 1 nm/Pt 9 nm/PtMn 50 nm/FePt 10–50 nm and Si//SiO_2/Fe 1 nm/Pt 9 nm/PtMn 50 nm/Pt 10 nm/FePt 10–50 nm. Samples were annealed at 300°C for 2 hours under a 3000 Oe external field.

coercivity because both samples have the same degree of Mn diffusion.

4.3 Summary

The ordering temperature of FePt films grown on PtMn underlayers was reduced due to phase transformation of the PtMn $L1_0$ phase. Since PtMn is ordered at a lower temperature than FePt, lattice changes of PtMn during annealing induce ordering of FePt at low temperatures. Furthermore, PtMn may provide extra anisotropy energy due to exchange-bias coupling. This enhancement is quite significant at FePt thicknesses less than 15 nm.

Although this chapter shows enhancement of in-plane FePt coercivity, the same concept can be applied to increase perpendicular coercivity if a proper underlayer or substrate, such as CrRu or MgO, was used to deposition of PtMn to develop a (002) texture of FePt. The perpendicular behavior discusses in the

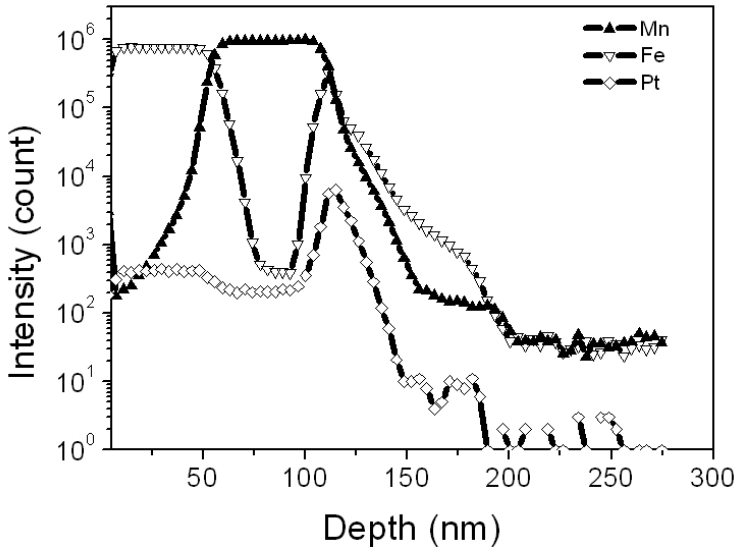

Figure 4.6: SIMS results of the structure Si//SiO2/Fe 1 nm/Pt 9 nm/PtMn 50 nm/FePt 50 nm. Samples were annealed at 300°for 2 hours.

next chapter.

Chapter 5

The morphology and switching behavior of perpendicular $L1_0$ FePt with PtMn underlayer

The perpendicular ordered FePt films have been successfully fabricated on MgO substrates. As discussed in the pervious chapter, the ordered phase of antiferromagnetic PtMn is a $L1_0$ phase, the same as FePt. The a-axis lattice constants of the ordered PtMn is 0.40 nm which is very close to the one of FePt. Therefore, PtMn is a very suitable underlayer for epitaxial growth of FePt. Furthermore, at high temperature process, the Mn may diffuse into the FePt layer and form the FeMnPt ternary alloy. As the increase of Mn content, the saturated magnetization and anisotropy constant decrease. The $(Fe_{1-x}Mn_x)Pt$ becomes antiferromagnetic while the Mn content reach 0.68[51]. Hence, the diffusion of Mn may change the switching behavior of the FePt.

5.1 Experiment

Samples with the structure of MgO (001)//FePt x nm and MgO (001)//PtMn 50 nm/FePt x nm (x = 12.5, 25, 50) were prepared at 500°C. FePt and PtMn were deposited by co-sputtering two elemental targets. The compositions were controlled by the deposition power and verified by using inductively coupled plasma-mass spectrometer (ICP-MS). The compositions of the single layer of FePt and PtMn are $Fe_{52}Pt_{48}$ and $Pt_{49}Mn_{51}$, respectively.Hysteresis loops were measured using a vibrating sample magnetometer (VSM). First order reversal curves (FORC) diagram was used to analyze the switching behavior. X-ray diffraction (XRD) using the Cu K_α line was performed to identify the structures.

5.2 Results and discussion

Figure 5.1 shows the x-ray $\theta - 2\theta$ scan of samples with and without PtMn underlayer at different FePt thickness. The figure 5.1 (a), the pure FePt directly deposit on MgO (001) substrate, shows a very good (001) textual growth. No FePt (111) peak was found in the scan and the peak intensity increased as the thickness of the FePt increased. On the other hand, all samples with PtMn underlayer also show a good (001) textual growth. No (111) peaks were found in the scan for both PtMn and FePt. Although the FePt (001) and (002) peak intensity increased as the thickness of FePt increase, the PtMn (001) and (002) peak intensity decreased. This maybe due to the inter diffusion of FePt and PtMn during the high temperature process. Even though the diffusion may occur, all samples still keep a very good (001) prefer orientation.

In order to confirm whether the PtMn and FePt is epitaxial growth, the x-ray ϕ scans of the [111] peak were preformed. Figure 5.2 shows the ϕ scan

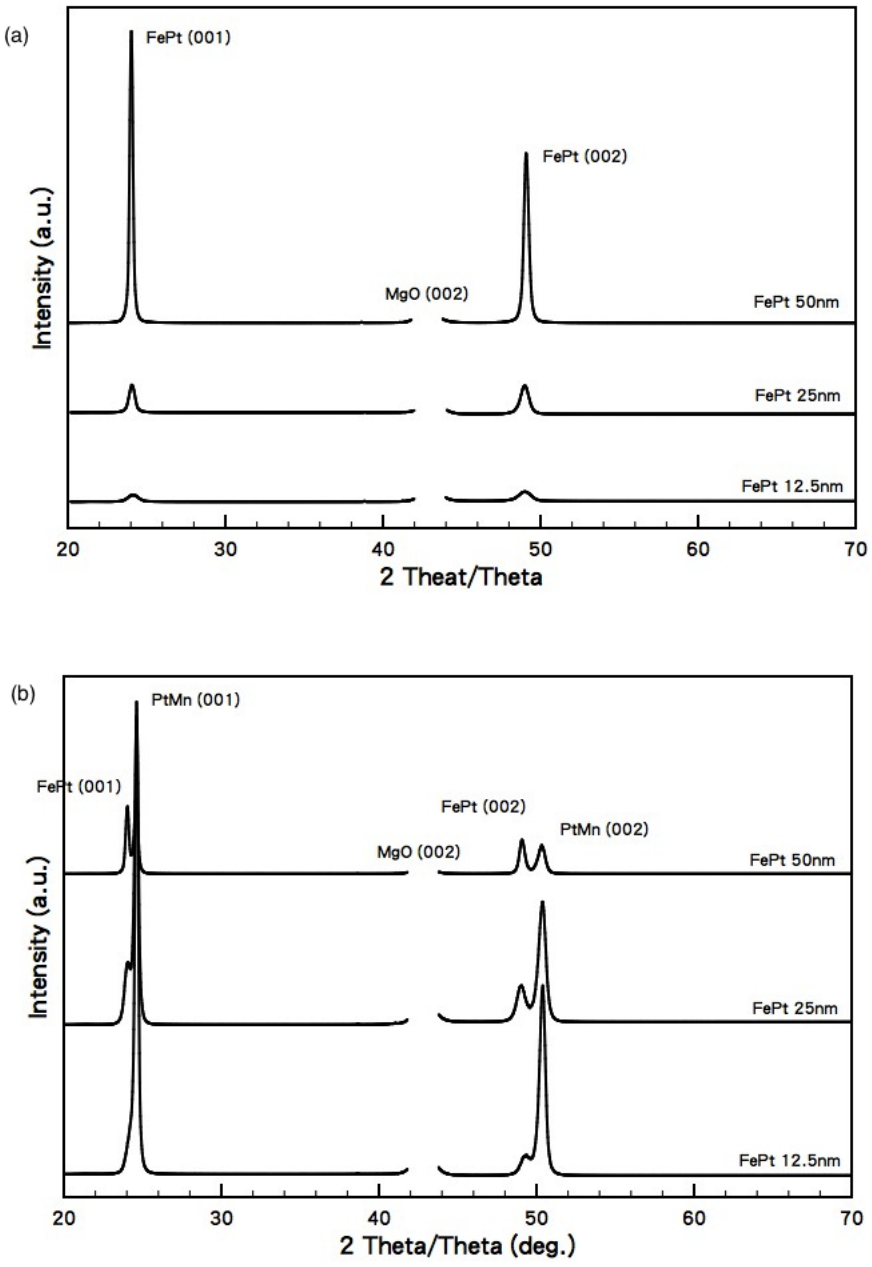

Figure 5.1: The XRD 2θ scan of (a) MgO (001)//FePt x nm and (b) MgO (001)//PtMn 50 nm/FePt x nm (x = 12.5, 25, 50) as-deposit films.

results of MgO (001)//FePt 50 nm and MgO (001)//PtMn 50 nm/FePt 50 nm, all observed peaks of FePt and PtMn were separated by 90°. This shows fourfold symmetry corresponds to an epitaxial relationship with direct cubic on cubic structure. i.e., the [100] and [010] directions of FePt, PtMn and MgO are aligned. This also proves that the diffusion of Mn into FePt film does not destroy the epitaxial growth.

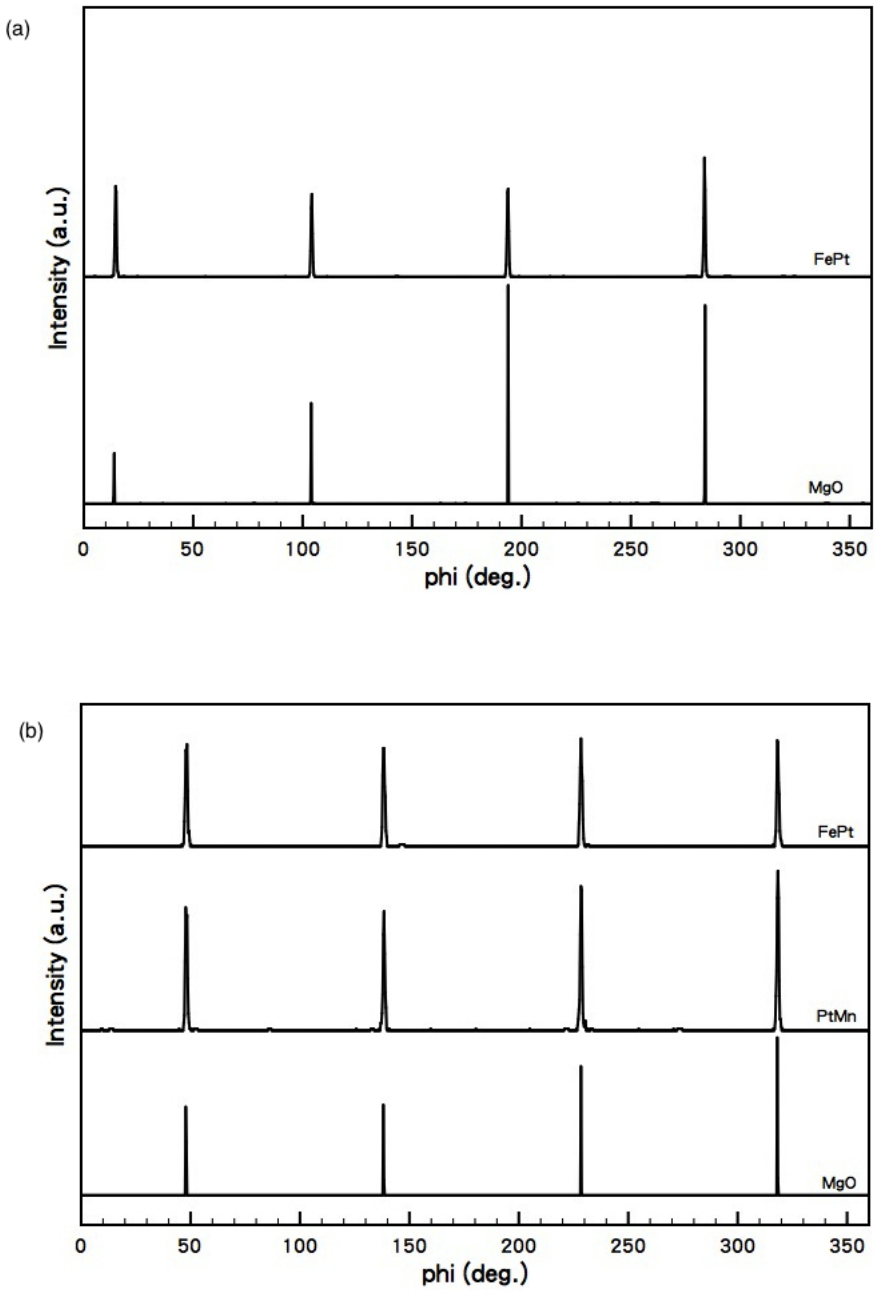

Figure 5.2: The XRD ϕ scan of the [111] peak of (a) MgO (001)//FePt 50 nm and (b) MgO (001)//PtMn 50 nm/FePt 50 nm as-deposit films.

The evolution of the morphology and the corresponding magnetic domain structure with increasing the FePt thickness are shown in figure 5.3 and figure 5.4. The FePt growth on the MgO substrate start with a thin layer with holes (shown in figure 5.3 (a)). As the thickness of FePt increase to 25nm, the FePt shows a clear island growth shown in figure 5.3 (b). Finally, as the thickness of FePt increases to 50nm, all the islands merge together and form a continuous film with holes in it (figure 5.3 (c)). As the thickness of FePt increase, the FePt islands become larger and eventually marge together. The boundaries of the islands become holes as the islands merged. These holes may become pinning sites of the domain wall. The MFM images all show similar structure which are common in the perpendicular magnetic films.

For samples with PtMn underlayer, the FePt island become cubic shape as shown in figure 5.4 (a). This kind of cube morphology may be due to the smaller lattice mismatch of PtMn and FePt. For smaller lattice mismatch, the FePt may form a larger and better separated islands with definite faceting edge[54]. These orthogonal edges become pinning site of the domain wall and thus form a special domain structure as shown in figure 5.4 (d), (e) and (f). As the thickness of FePt increase, the cubes merge to each other. However, even when the FePt thickness reached 50nm, the orthogonal edge were still quite noticable. Therefore, the MFM image of FePt 50nm on PtMn shows a mosaic pattern as shown in figure 5.4 (f).

The hysteresis loops are shown in the figure 5.5. Figure 5.5 (a), (b) and (c) are the loops of FePt directly deposited onto the MgO (001) substrate without PtMn layer. On the other hand, figure 5.5 (d), (e) and (f) are those of the samples with PtMn underlayer. All samples show good perpendicular anisotropy which consist with the x-ray results. For samples without PtMn

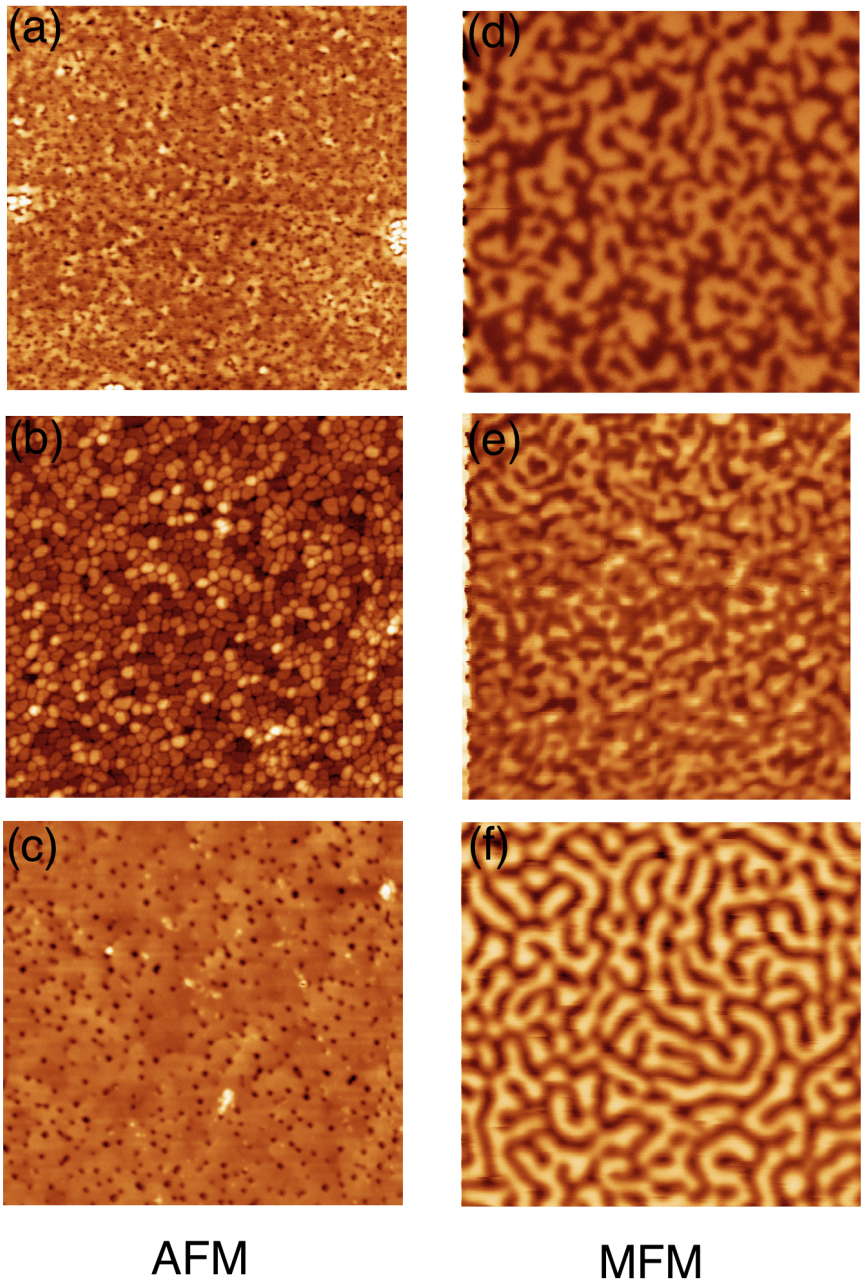

Figure 5.3: AFM and MFM images of (a) (d) FePt 12.5nm, (b) (e) FePt 25nm and (c) (f) FePt 50nm without PtMn underlayer. The scan range is $5 \times 5 \mu m$. The MFM images are taken at the de-magnetization state.

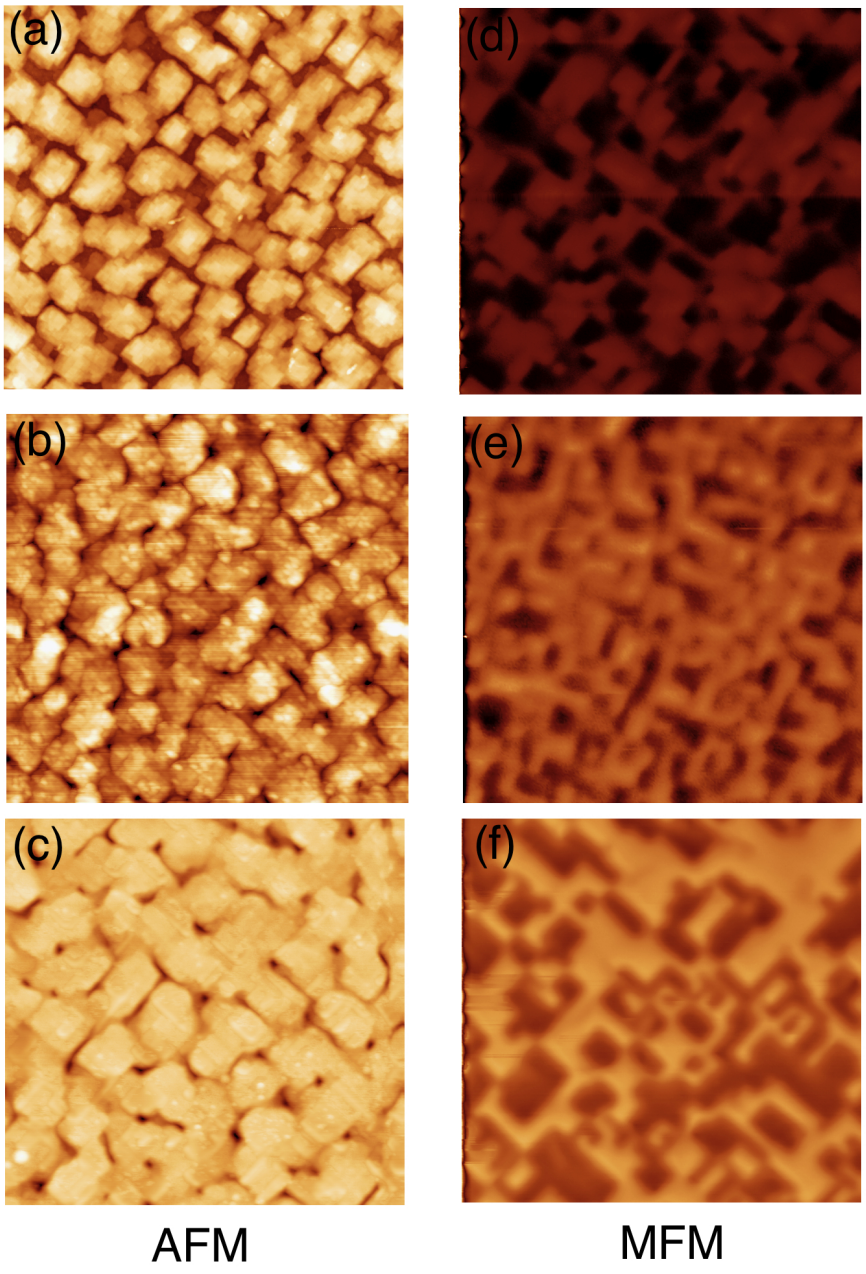

Figure 5.4: AFM and MFM images of (a) (d) FePt 12.5nm, (b) (e) FePt 25nm and (c) (f) FePt 50nm with PtMn underlayer. The scan range is $5 \times 5 \mu m$. The MFM images are taken at the de-magnetization state.

underlayer, the switching is very sharp. The sudden drop of the coercivity as the FePt thickness increased to 50nm (as shown in figure 5.5(c)) results from the formation of the strip domain. The switching of the sample becomes blunter with PtMn underlayer than that of the samples than the samples without PtMn underlayer. Moreover, the in-plane hysteresis loops start to show small loops at low field, which indicate that some soft magnetic phases is formed. For the FePt thickness of 50nm case (shown in figure 5.5(f)) the switching shows two-step switching. The magnetization begins to be reversed as the applied field just pass the zero, indicating the reversal of the soft phase. At the field of 2000 Oe, the reversal becomes faster, representing the hard layer reversal. The sharp switching implaies that all samples with PtMn underlayer is a domain wall motion type switching. The coercivity of samples with PtMn underlayer is larger than that of samples without PtMn underlayer. The enhancement of coercivity may result from the extra pinning or the exchange coupling provide by the PtMn. The MFM images of samples with PtMn underlayer (figure 5.4), the domain walls are mostly pinned along the orthogonal edges. Therefore, those edges provide more pinning sites than those holes on the samples without PtMn underlayer.

In order to further investigate the switching behavior of the samples, first order reversal curve (FORC) analysis was performed. FORC diagram provides a detailed characterization of the hysteretic response of a magnetic system to an applied field. The FORC analysis capture about 10^2 reversal curves, each starting at successively more negative reversal fields, H_R and measured with an increasing applied field H perpendicular to the film plane. Notice that the FORC measurement is very sensitive to the irreversible magnetization reversal. The FORCs and the corresponding FORC diagram of MgO//FePt 12.5nm are shown in figure 5.6. The positive peak around the field of 2000 Oe indicates

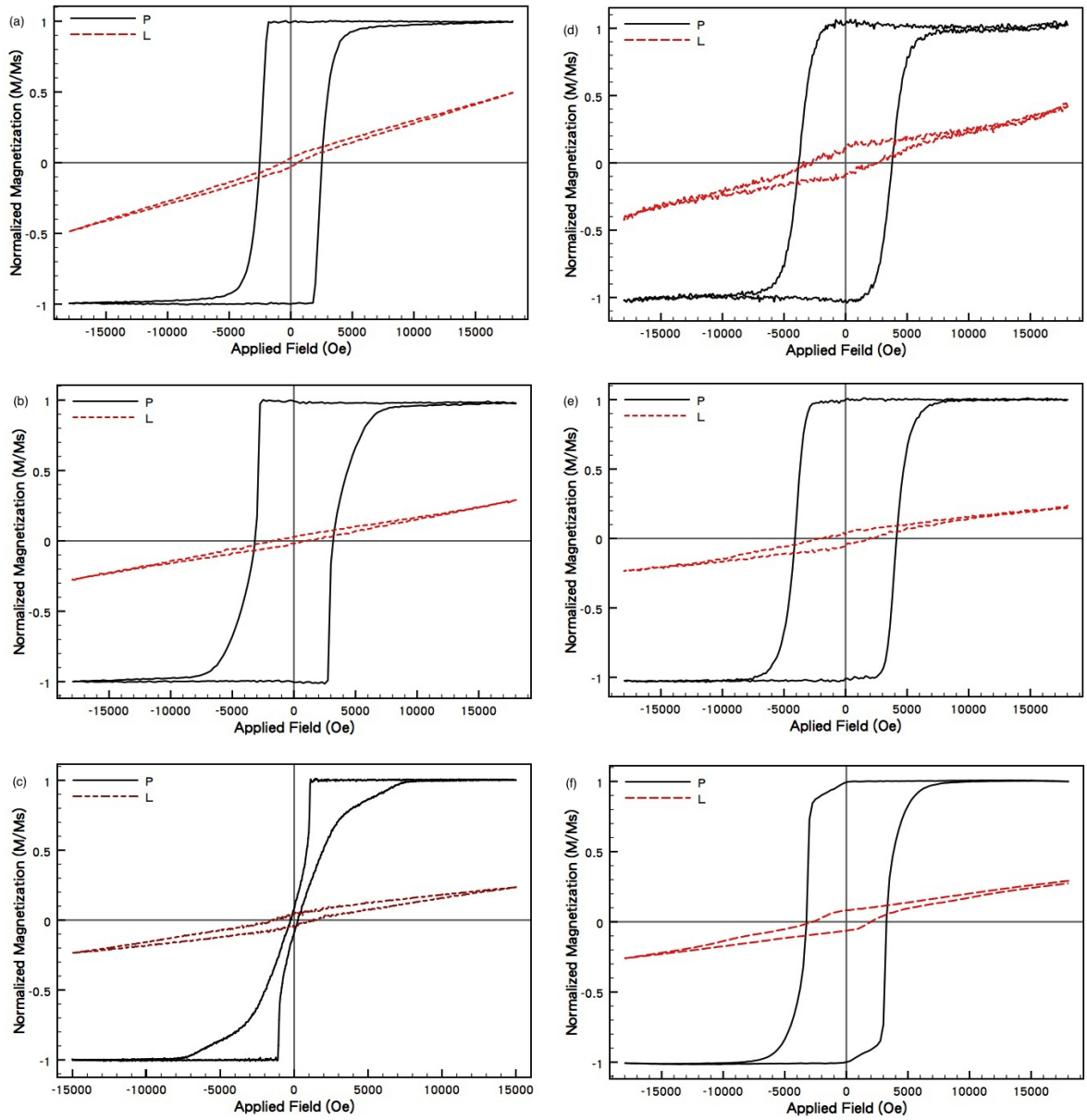

Figure 5.5: The perpendicular and longitudinal hysteresis loops for (a) FePt 12.5nm (b) FePt 25nm (c) FePt 50nm (d) PtMn 50nm / FePt 12.5nm (e) PtMn 50nm / FePt 25nm and (f) PtMn 50nm / FePt 50nm deposited on the MgO (001) substrate.

the domain wall nucleation, and the positive-negative pair of distributions in the FORC diagram indicates the irreversible domain annihilation. This kind of shape on the FORC diagram (shown in figure 5.6 (b)) represent the domain wall motion type of switching.

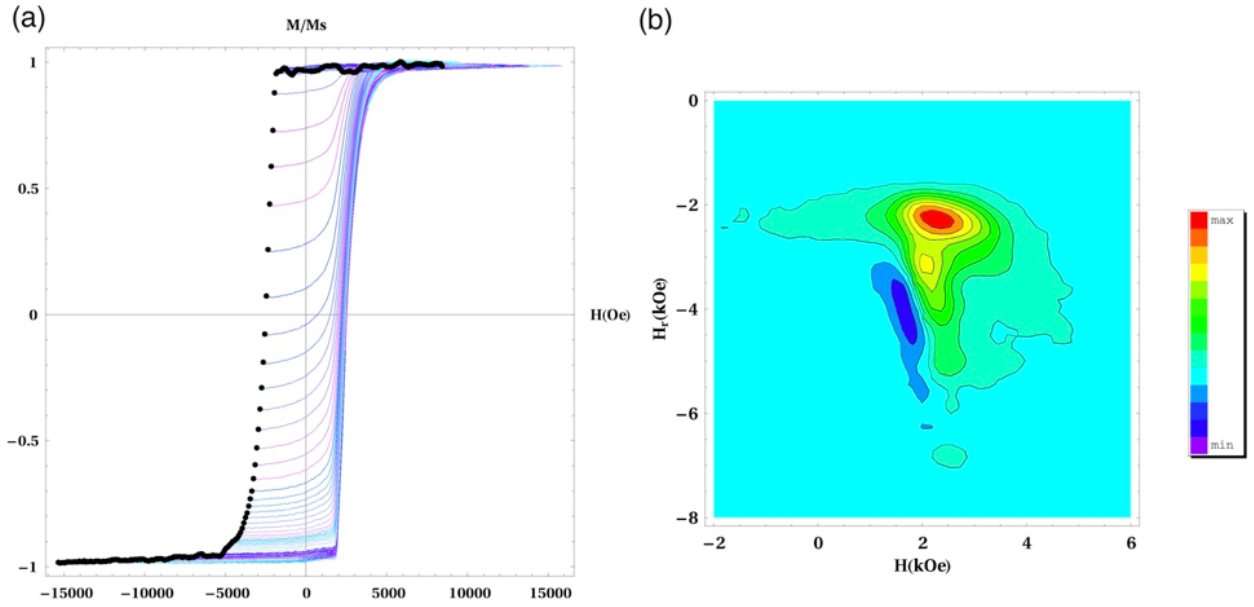

Figure 5.6: (a) FORCs and (b) FORC diagram of MgO//FePt 12.5nm.

Figure 5.7 shows FORCs and FORC diagram of FePt 12.5nm with PtMn underlayer. The large single peak indicates that the switching is rotation dominant. Unlike the case without PtMn underlayer, positive peak spread to a large range of field which indicates that the interactions between hysterons are weaker. This may be due to the morphology change while inserting the PtMn layer. The growth of FePt with PtMn underlayer is the separated cubic island as shown in figure 5.4 (a). On the contrary, the FePt without the PtMn underlayer is more like continuous film (see figure 5.3 (a)). Therefore, the separation of the islands reduces the interaction between the islands.

As the thickness of FePt reaches 25nm, both samples with and without underlayer show typical positive-negative pair of distributions which indicates

the irreversible domain annihilation (shown in figure 5.8 and figure 5.9). However, the broadened positive peak observed for samples with the PtMn layer indicates that there are some rotation type switching mixed in the reversal. On the other hand, the sample without PtMn underlayer shows clear domain wall motion type reversal. When thickness is increased the islands merge to each other. Thus, the interaction between islands become larger.

Figure 5.10 shows the FORCs and FORC diagram of MgO//FePt 50nm. Three stages of reversal with distinct features in both the hysteresis loop and the FORC diagram are observed: an initial rapid and irreversible domain propagation from already nucleated sites which leads to a precipitous drop in the magnetization and a horizontal ridge in the FORC diagram; a subsequent mostly reversible process of domain width expansion-contraction with little change in the domain morphology, which corresponds to gradual changes in magnetization; and an irreversible domain annihilation process, when reaching negative saturation, thus yielding a vertical negative-positive pair of peaks in the FORC diagram. This set of FORC patterns is characteristic of the vertically correlated magnetization reversal[55].

For sample of 50nm FePt with PtMn underlayer, there is a shoulder shown in the hysteresis loop (as seen in figure 5.11 (a)) indicating the soft phase reversal. As shown in figure 5.11 (b), there are no peaks shown in the FORC diagram. Notice that, only the irreversible process can be shown on the FORC diagram. Therefore, the reverse of the soft layer is a reversible process which fit in the characteristics of the exchange coupled control (ECC) media. More discussion on the soft and hard layer switching in the next chapter.

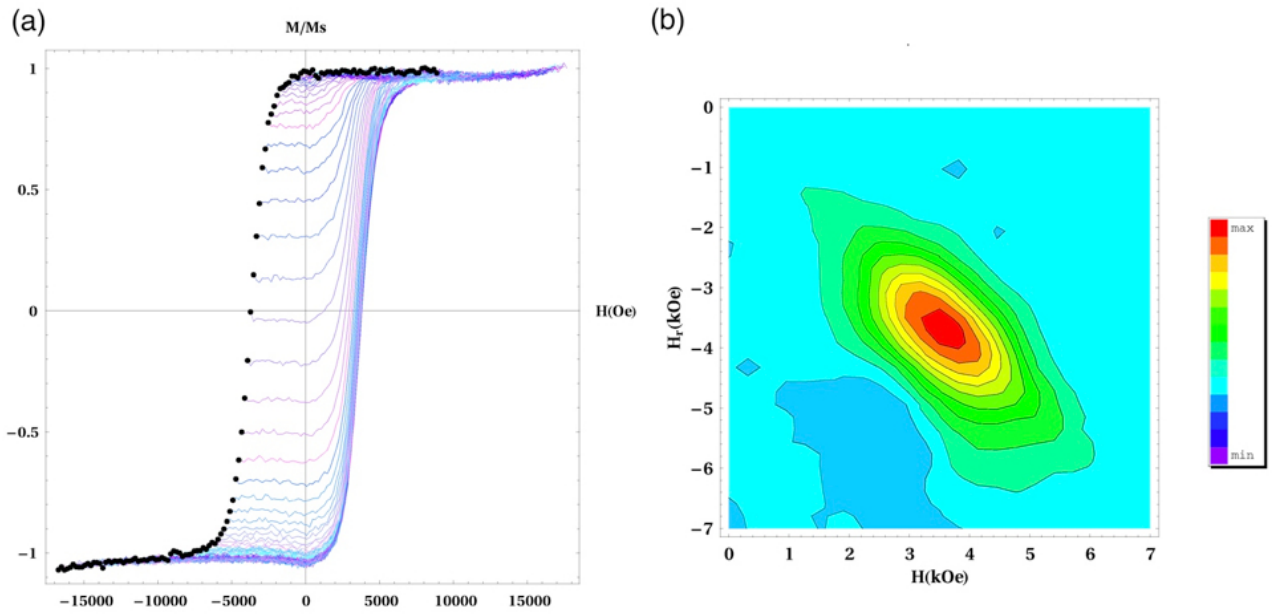

Figure 5.7: (a) FORCs and (b) FORC diagram of MgO//PtMn 50nm/FePt 12.5nm.

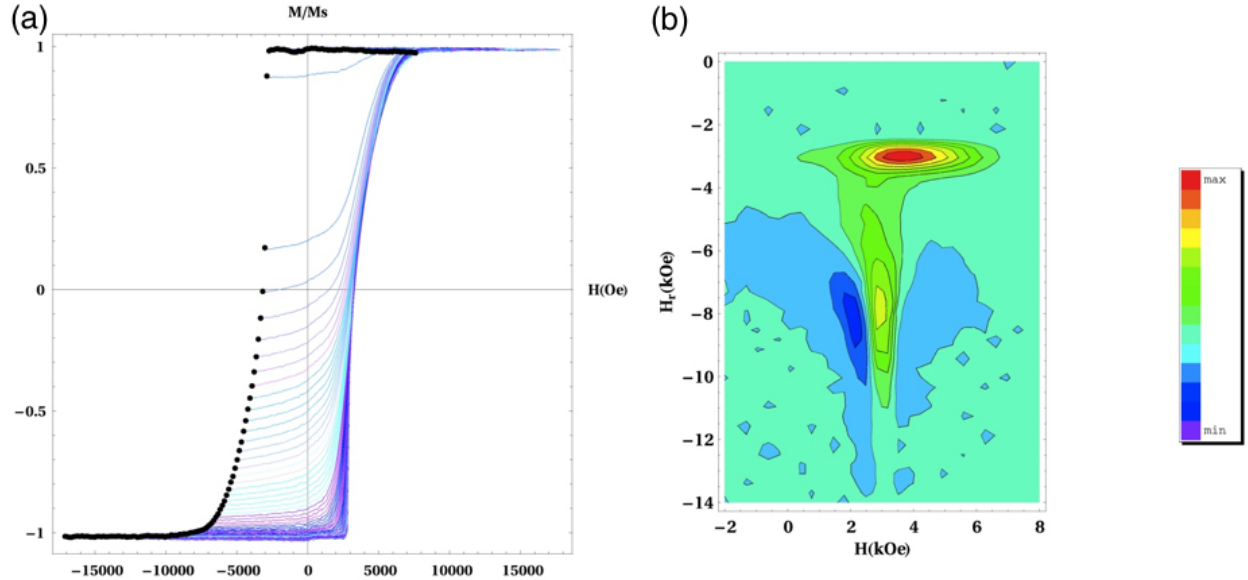

Figure 5.8: (a) FORCs and (b) FORC diagram of MgO//FePt 25nm.

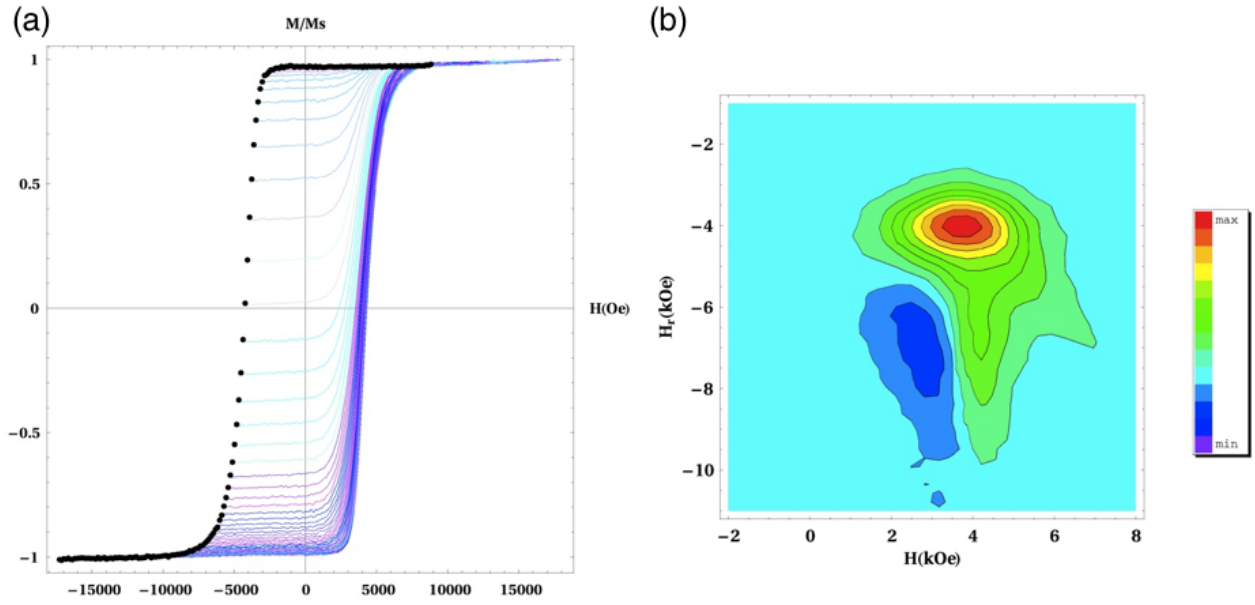

Figure 5.9: (a) FORCs and (b) FORC diagram of MgO//PtMn 50nm/FePt 25nm.

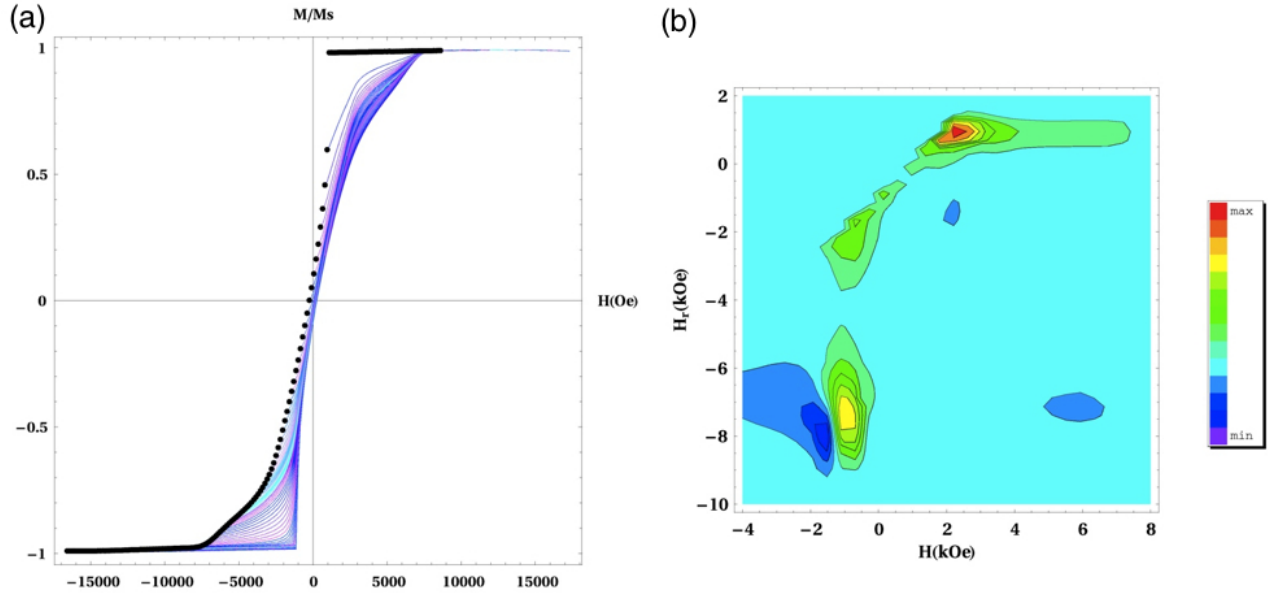

Figure 5.10: (a) FORCs and (b) FORC diagram of MgO//FePt 50nm.

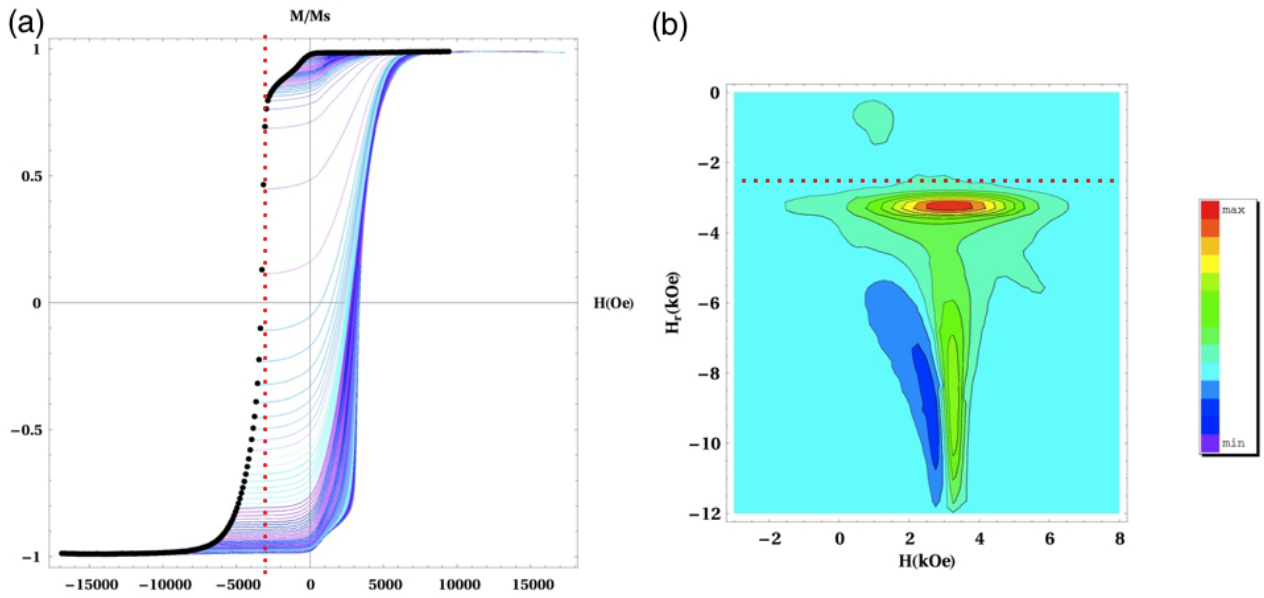

Figure 5.11: (a) FORCs and (b) FORC diagram of MgO//PtMn 50nm/FePt 50nm. The red dot lines indicates the beginning of the irreversible reversal.

5.3 Summary

In summary, the (001) FePt can epitaxially grow on the PtMn underlayer. The presence of PtMn eliminates the strip domains, observed in (001) FePt directly grown on MgO, and forms special rectangular domains. As the thickness of the FePt increase, the switching behavior of samples with PtMn underlayer change from rotation dominant type to the domain wall motion dominant type. On the contrary, samples without PtMn layer show domain wall motion dominant type for all thickness we studied. However, as the thickness of FePt reaches 50nm, the sample shows strong vertically correlated magnetization reversal. The coercivity of all samples are enhanced by inserting the PtMn layer. The enhanced coercivity is related to the pinning sites created by the special morphology from PtMn underlayer.

Chapter 6

The PtMn/FePt graded media

To achieve high-density magnetic recording, high anisotropy materials are required to maintain thermal stability; on the other hand, an affordable writing field is limited so several schemes have been investigated, including tilted, exchange coupled composite (ECC), graded, patterned media and energy assisted recording. Among these approaches, graded media with continuously varied anisotropy are quite attractive because the switching field can be significantly reduced while the thermal stability of media remains the same. Graded media are predicted to provide additional gains in writabilty over conventional bi-layer hard/soft ECC media[56–59].

As discussed in pervious chapter, some soft phase form in samples with PtMn underlayer. The PtMn underlayer is used for achieving (001)-growth of FePt films and at the same time serves as the diffusion source of Mn for the composition gradient. The formation of the soft phase may due to the diffusion of the Mn and thus make the FePt become graded media. In high temperature process, the Mn may diffuse into the FePt layer and form the FeMnPt ternary alloy. As the increase of Mn content, the saturated magnetization and anisotropy constant decrease. The $(Fe_{1-x}Mn_x)Pt$ becomes antiferromagnetic while the Mn

content reach 0.68[51]. Furthermore, the exchange coupling between antiferromagnetic PtMn and ferromagnetic FePt introduces extra anisotropy, and thus enhances coercivity of FePt. The extra anisotropy origination from the exchange coupling decreases with the distance away from the interface. Here, we tried to verify that PtMn/FePt bilayers behave as graded media.

6.1 Experiment

The sample preparation is the same as previous chapter. The depth profiles of compositions were verified by a auger electron spectroscopy (AES) depth analysis. Polarized neutron reflectometry (PNR) and X-ray magnetic circular dichroism (XMCD) measurements show gradation in magnetic anisotropy, and that this anisotropy gradient facilitates domain nucleation upon magnetization reversal.

6.2 Results and discussion

First, in order to study the concentration profile of the sample after deposition, the Auger electron spectroscopy depth profile was performed. The result, shown in Figure 6.1, indicates that Mn diffuse a lot into the FePt layer and form a concentration gradient which may result in a graded media.

To further investigate how the diffusion of the Mn atoms affects the depth-dependent magnetization reversal, we on purpose doped small amount of Co at the different depth positions of the FePt layer and performed XMCD measurements to obtain the local hysteresis loop. We prepared three samples of MgO//PtMn 50nm/FePt 25nm in which Co (nominal thickness of 1nm) was

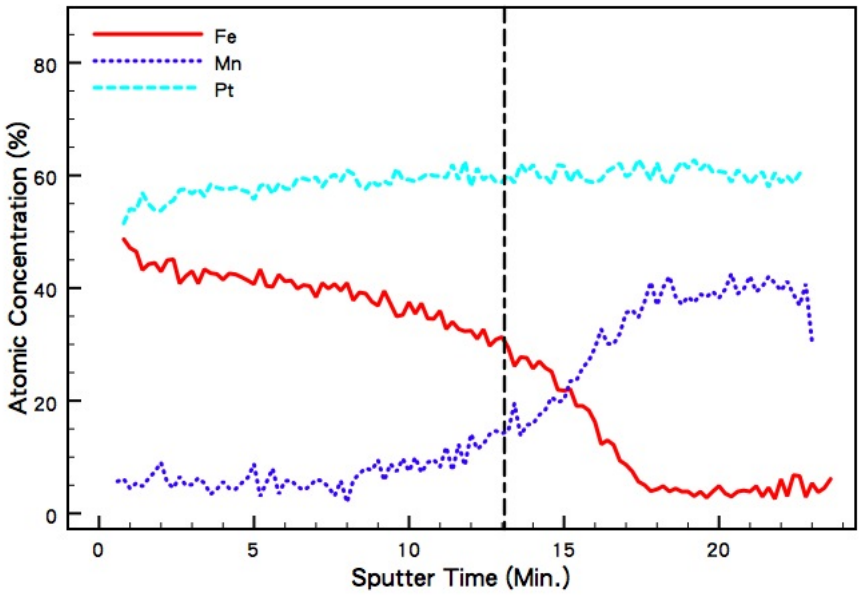

Figure 6.1: The AES depth profile of MgO//PtMn 50nm/FePt 50nm. The dash line indicate the layer boundary between FePt and PtMn.

co-sputtered with FePt at the designated depth, away from the most top surface, of 21 nm (bottom), 14 nm (middle) and 5 nm (top), respectively. XMCD measurements were performed at the Dragon beam line 11A at the National Synchrotron Radiation Research Center (NSRRC) in Taiwan. The element-specific XMCD loops of the Co-marker layer, measured at Co L_3 edge, were obtained by using the fluorescence yield mode Since Co-marker should strongly couple to the local FePt, the perpendicular loops of Co-marker could be used as the indicator of local magnetization reversal in FePt15. Figure 6.2 shows hysteresis loops for Co doped at different depth measured by using VSM and XMCD. The VSM loops, which give the total magnetic signal from the sample, for three samples are almost the same. Although XMCD loops are relatively noisy due to quite limited amount of Co, they reveal that the Co doped at the middle shows the lowest coercivity rather than doped at bottom case in which more Mn atoms existed. On the other hand, the similar reference samples without the PtMn underlayer showed identical Co loops measured by both XMCD

and VSM regardless of the positions of Co doping (shown in figure 6.3).

Two effects have to be taken into consideration. First, it is known and discussed in pervious chapter that the presence of antiferromagnetic layer could provide an extra exchange coupling to stabilize the magnetic layer. However, since the exchange coupling is an interfacial phenomenon, its strength decreases with increasing the distance away from the interface of FePt/PtMn. Second, the diffusion of Mn may lead to variations of FePt anisotropy due to the formation of the $(Fe_{1-x}Mn_x)Pt$ alloy. The more the Mn composition is, the smaller the anisotropy of the ferromagnetic $(Fe_{1-x}Mn_x)Pt$ is. As a result, in the region near the interface of FePt/PtMn, the Mn content is high enough to form antiferromagnetic $(Mn_{1-x}Fe_x)Pt$ so exchange coupling still exists. The competition between Mn alloying and exchange coupling explains the observed XMCD loops: at the bottom of FePt layer, the anisotropy is enhanced by the exchange coupling to $(Mn_{1-x}Fe_x)Pt$. For the middle of the FePt layer, the exchange coupling strength becomes weaker and the anisotropy is reduced by the existence of Mn so the effective anisotropy is the smallest. At the top of the FePt layer, due to the less content of Mn, the anisotropy is increased.

In order to further determine the depth-dependent magnetic anisotropy gradient and confirm the special behavior observed by the XMCD which is not due to the Co doping, the samples were studied by PNR. PNR is sensitive to magnetic profiles of thin films and multilayers. Notice that the PNR is sensitive only to the in-plane magnetization and is totally insensitive to magnetization normal to the sample surface[60,61]. We first saturate the sample in perpendicular direction then perform the PNR measurement while apply a 800mT field in the direction parallel to the sample surface. From the in-plane magnetization profile, we are able to see how magnetic moment at different depth be pulled

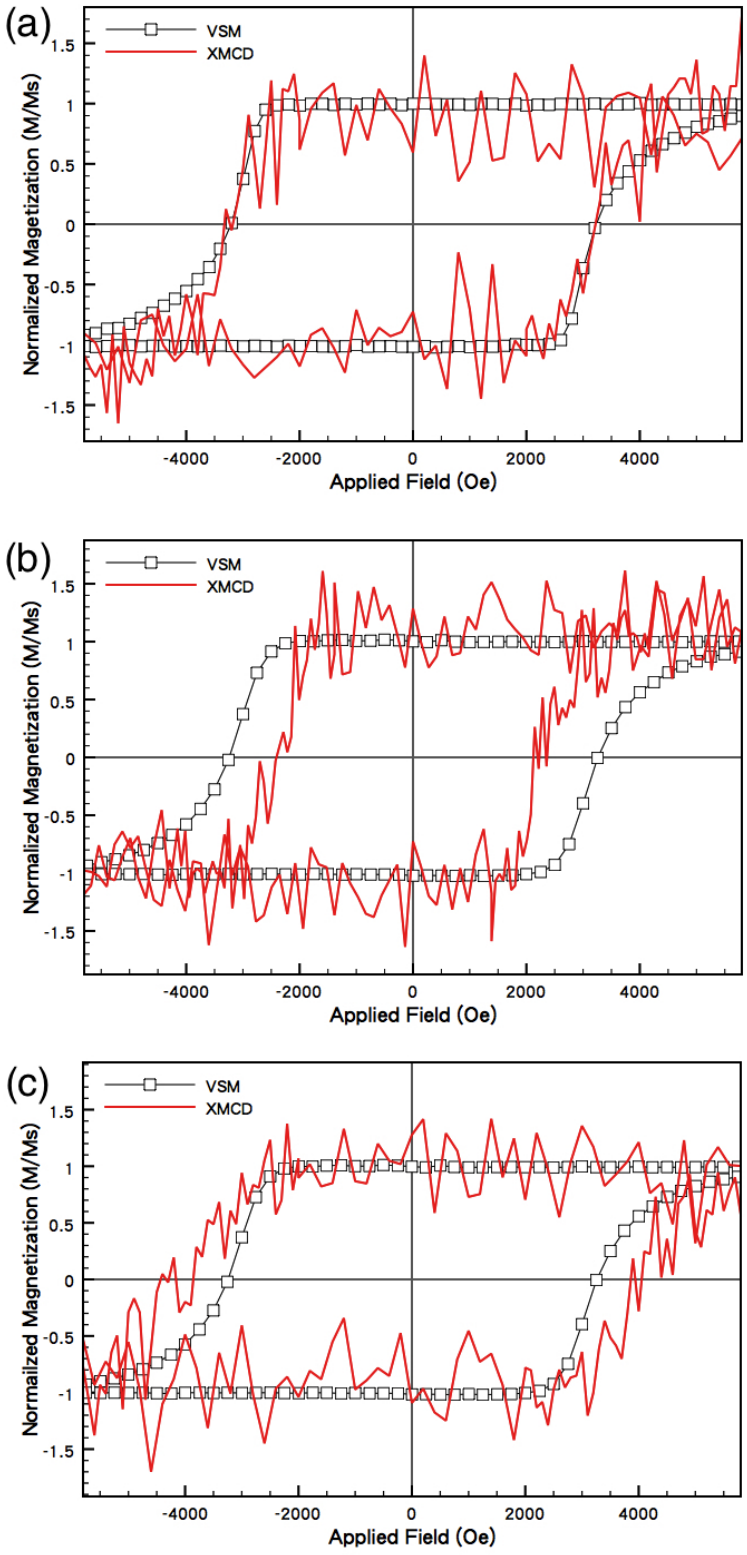

Figure 6.2: The hysteresis loops and XMCD loops for Co dope at (a) top, (b) middle and (c) bottom of FePt 25nm sample with PtMn underlayer.

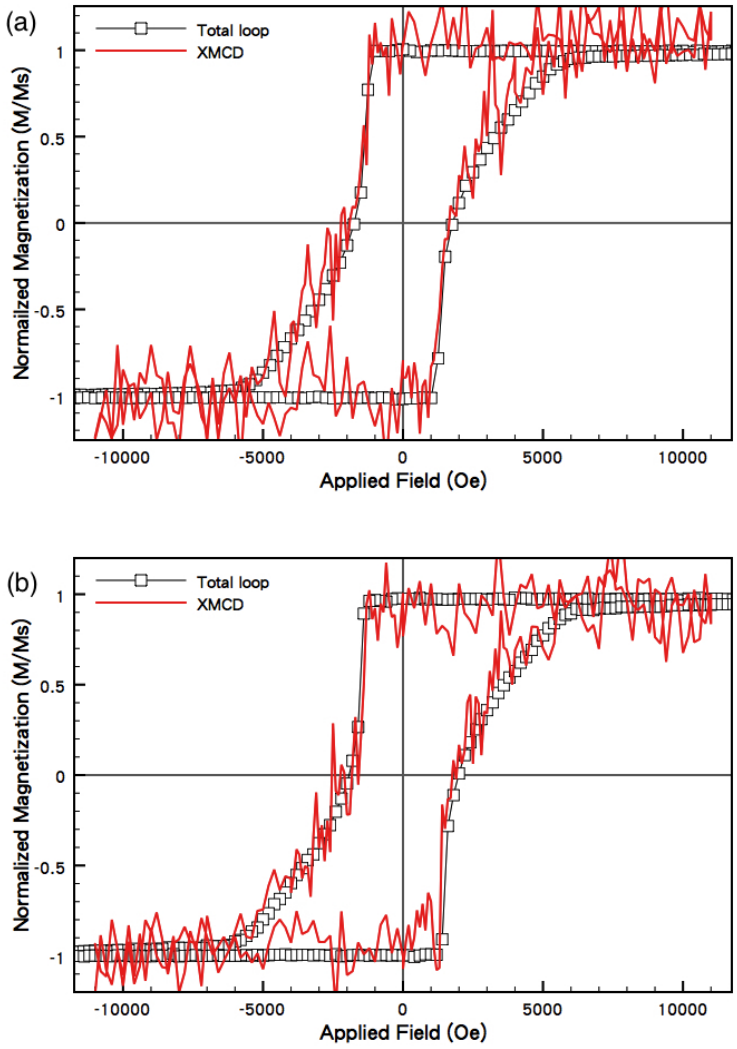

Figure 6.3: The hysteresis loops and XMCD loops for Co dope at (a) top and (b) middle of FePt 25nm sample without PtMn underlayer.

away from the perpendicular easy-axis direction. Thus, we can equate this magnetic depth profile with the anisotropy profile. PNR measurements were conducted using the NG-1 Reflectometer at the National Institute of Standards and Technology (NIST) Center for Neutron Research. An incident monochromatic neutron beam was polarized to be alternately spin up or down relative to H. The non-spin-flip reflectivity (with incident beam spin up or down) and the spin-flip reflectivity (up to down and down to up) were measured as functions of the scattering vector Q. The samples' depth-dependent nuclear scattering length density profiles $\rho_{N(z)}$ (functions of the scattering potential of the constituent nuclei at different depths z beneath the sample surface) and M(z) profiles were determined by model fitting the PNR data, using exact dynamical calculations[62]. Measurements were performed at room temperature.

The depth-dependent in-plane magnetization projection M(z) profile is shown in figure 6.4. The magnetic profile was measured under in-plane 800mT field after saturated at out-of-plane. The in-plane magnetization exhibits largest magnetization at the middle of the magnetic layer which conforms to the XMCD data. This result may due to the extra anisotropy provide by the PtMn antiferromagnetic layer. In Mn rich region, the FePtMn ternary alloy is antiferromagnet. On the other hand, the Fe rich region is ferromagnet[52]. Therefore, it is a competition between the decrease of anisotropy due to the Mn diffusion in ferromagnetic part and the increase extra anisotropy because of the formation of antiferromagnetic phase. Consequently, the diffusion of Mn into FePt layer results in a special graded media which the magnetic soft layer is in the middle. The reverse domain first form in the middle of the film and then propagate up and down to complete the switching.

We further demonstrate that we can utilize the Mn concentration profile

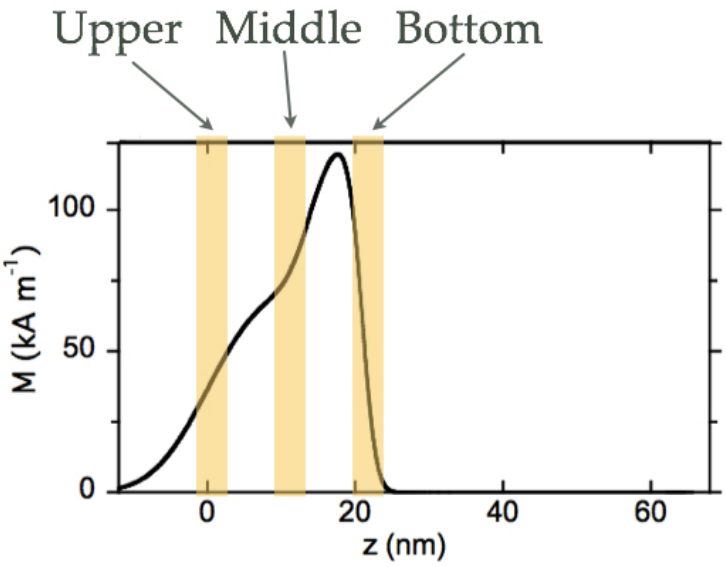

Figure 6.4: The magnetic profile form the PNR. The marks indicate the corresponding Co doping in XMCD experiment.

and exchange coupling from the PtMn layer to adjust anisotropy profile of FePt to create the characteristic we want. By further combining different annealing process, we can achieve desired anisotropy profile. For example, we can fabricate a strong graded soft layer at the bottom and a high-anisotropy hard layer on the top. The layer structure was still the same (MgO//PtMn 50nm/FePt 25nm) but after depositing first FePt 20nm layer at 500°C, the sample was in-situ annealed at 550°C for 30min to promote the Mn diffusion. After annealing, the last 5nm FePt was deposited. As shown in figure 6.5, the AES depth profile showed a Mn poor region near the top surface and the Mn concentration in the first 20 nm was increased (figure 6.5 (b)) compared with the sample without annealing (figure 6.5 (a)).

We employed the first order reversal curves (FORCs) to study the reversal behavior of the sample. Families of FORCs and the corresponding FORC distribution are shown in . The FORC distribution shown in figure 6.6 (b) is the typical case for soft-hard coupling, which has been reported in the cases

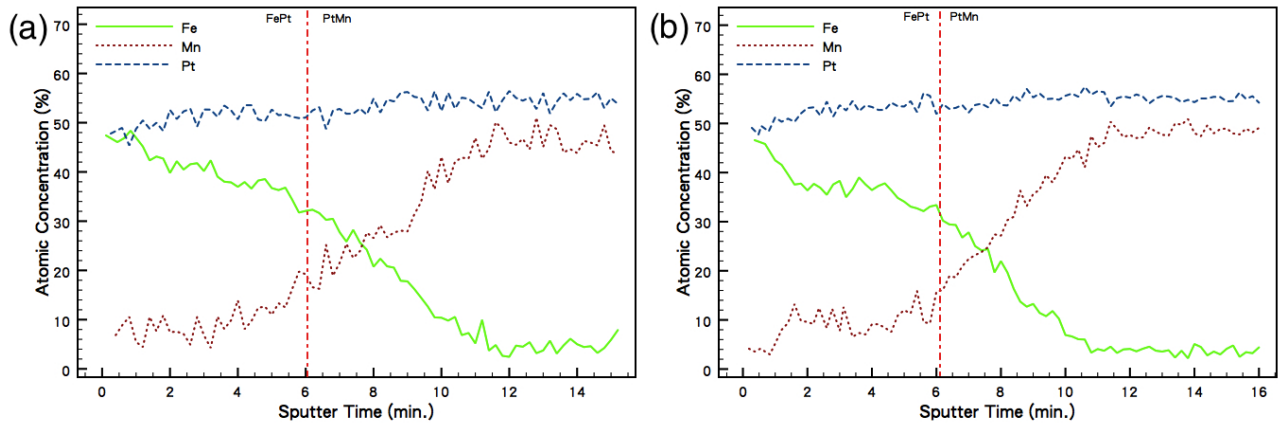

Figure 6.5: The AES depth profile of (a) MgO//PtMn 50nm/FePt 25nm and (b) MgO//PtMn 50nm/FePt 20 nm (in-situ annealed at 550°C)/FePt 5nm. The dash line indicate the layer boundary between FePt and PtMn.

of exchange-spring magnet and graded media[55]. A single and highly localized peak along with a pair of negative-positive tails was observed in the FORC distribution for the reversal field of H_R < -2500 Oe, suggesting the existence of both soft and hard phases. It should be noted that no appreciable feature was observed in the reversal field of H_R > -2500 Oe, which demonstrated the reversible reversal contributed from the soft phase coupled with the hard phase. By combining the FORC analysis with the AES depth profile and XMCD measurement, we confirms the existence of various anisotropy, or graded media, in our proposed structure of (001) FePt with PtMn underlayers.

6.3 Summary

In summary, we demonstrate that (001)-FePt graded media is successfully fabricated by using the PtMn underlayer. The PtMn underlayer provides a (001) structural template due to the similar lattice structure to FePt and supplies Mn source to achieve composition gradient; therefore, (001) FePt graded media can

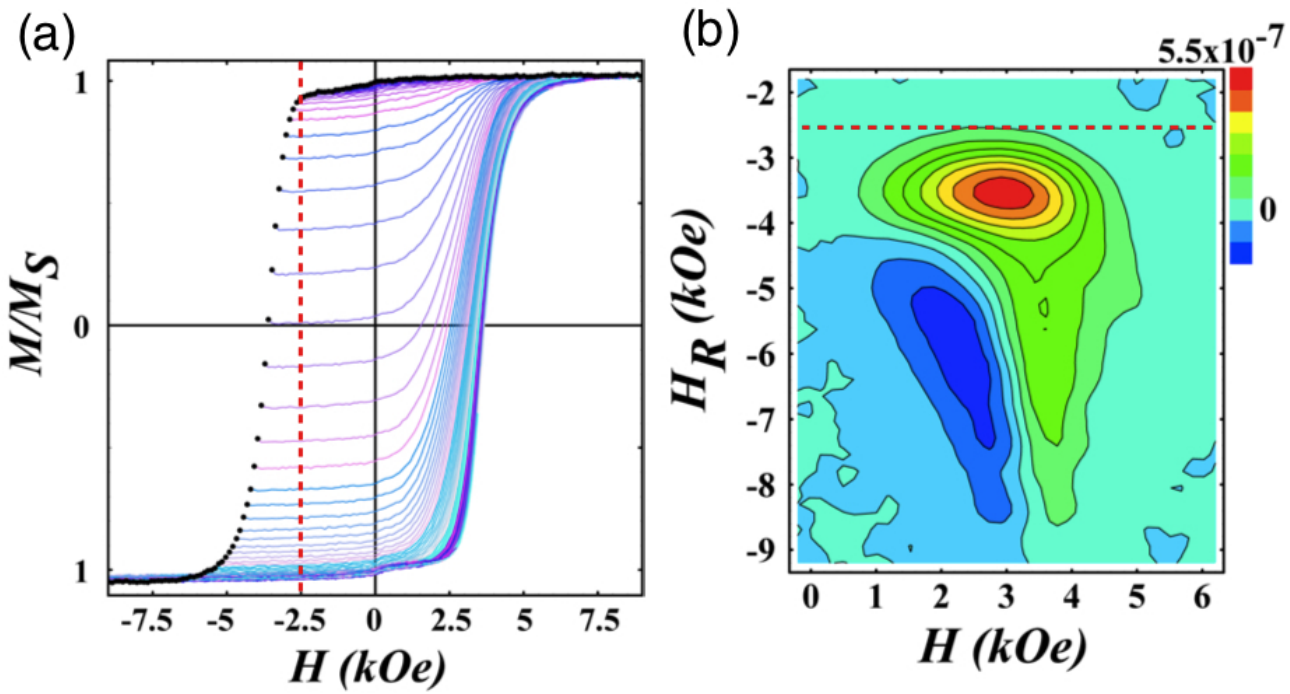

Figure 6.6: (a) Families of FORC's of MgO//PtMn 50nm/FePt 20 nm (in-situ annealed at 550°C)/FePt 5nm and (b) the corresponding FORC distribution. The red dash line indicates the beginning of the irreversible switching.

be obtained. We discover that the diffusion of Mn results in an unusual graded media from the X-ray magnetic circular dichroism and the polarized neutron reflectometry measurements. The anisotropy of FePt is varied by the effects of the exchange coupling to the antiferromagnetic PtMn and the formation of $(Fe_{1-x}Mn_x)Pt$ alloy.

Chapter 7

Conclusion

We use PtMn as the underlayer to grow FePt. The PtMn underlayer can induce ordering of FePt at low temperature. The ordering temperature of FePt films grown on PtMn underlayers was reduced due to phase transformation of the PtMn $L1_0$ phase. Since PtMn is ordered at a lower temperature than FePt, lattice changes of PtMn during annealing induce ordering of FePt at low temperatures. Furthermore, PtMn may provide extra anisotropy energy due to exchange-bias coupling. This enhancement is quite significant at FePt thicknesses less than 15 nm.

The PtMn is also a good underlayer for epitaxial growth of FePt on MgO (001) substrate. The presence of PtMn eliminates the strip domains, observed in (001) FePt directly grown on MgO, and forms special rectangular domains. As the thickness of the FePt increases, the switching behavior of samples with PtMn underlayer changes from rotation dominant type to the domain wall motion dominant type. On the contrary, samples without PtMn layer show domain wall motion dominant type for all thickness we studied. However, as the thickness of FePt reaches 50nm, sample show strong vertically correlated magnetization reversal. The coercivity of all samples is enhanced by inserting the

PtMn layer. The enhanced coercivity is related to the to the pinning sites created by the special morphology from PtMn underlayer. Also, we demonstrate that (001)-FePt graded media is successfully fabricated by using the PtMn underlayer. The PtMn underlayer provides a (001) structural template due to the similar lattice structure to FePt and supplies Mn source to achieve composition gradient; therefore, (001) FePt graded media can be obtained. We discover that the diffusion of Mn results in an unusual graded media from the X-ray magnetic circular dichroism and the polarized neutron reflectometry measurements. The anisotropy of FePt is varied by the effects of the exchange coupling to the antiferromagnetic PtMn and the formation of $(Fe_{1-x}Mn_x)Pt$ alloy.

By changing the MgO (001) single crystal substrate to MgO (001) textural film, we can integrate the PtMn/FePt graded media into the conventional recording media structure with a soft underlayer. It may be used in the future high density recording media.

References

[1] Weller, D. & Moser, A. Thermal effect limits in ultrahigh-density magnetic recording. *IEEE Trans. on Mag.* **35**, 4423–4439 (1999).

[2] Bennett, W., Zhang, B. & Richter, H. Influence of orientation ratio on reverse erase-edge noise and track-edge dipole distribution. *IEEE Trans. on Mag.* **34**, 743–749 (1998).

[3] Fullerton, E. *et al.* Antiferromagnetically coupled magnetic media layers for thermally stable high-density recording. *Appl. Phys. Lett.* **77**, 3806–3808 (2000).

[4] Abarra, E., Inomata, A., Sato, H., Okamoto, I. & Mizoshita, Y. Longitudinal magnetic recording media with thermal stabilization layers. *Appl. Phys. Lett.* **77**, 2581–2583 (2000).

[5] Iwasaki, S. Discoveries that guided the beginning of perpendicular magnetic recording. *J. Magn. Magn. Mater* **235**, 227–234 (2001).

[6] Ruigrok, J., Coehoorn, R., Cumpson, S. & Kesteren, H. Disk recording beyond 100 Gb/in^2: Hybrid recording? (invited). *J. Appl. Phys.* **87**, 5398–5403 (2000).

[7] New, R., Pease, R. & White, R. Lithographically patterned single-domain cobalt islands for high-density magnetic recording. *J. Magn. Magn. Mater* **155**, 140–145 (1996).

[8] Farrow, R. *et al.* Control of the axis of chemical ordering and magnetic anisotropy in epitaxial FePt films. *J. Appl. Phys.* **79**, 5967–5969 (1996).

[9] Maat, S. *et al.* Antiferromagnetic structure of $FePt_3$ films studied by neutron scattering. *Phys. Rev. B* **63**, 134426 (2001).

[10] Landau, L. D., Lifshitz, E. M. & Pitaevski, L. P. *Electrodynamics of Continuous Media* (Elsevier, 2004).

[11] Meiklejohn, W. & Bean, C. New magnetic ansiotropy. *Phys. Rev.* **102**, 1413–1414 (1956).

[12] Meiklejohn, W. & Bean, C. New magnetic ansiotropy. *Phys. Rev.* **105**, 904–913 (1957).

[13] Malozemoff, A. P. Random-field model of exchange anisotropy at rough ferromagnetic-antiferromagnetic interfaces. *Phys. Rev. B* **35**, 3679–3682 (1987).

[14] Mauri, D., Siegmann, H., Bagus, P. & Kay, E. Simple model for thin ferromagnetic films exchange coupled to an antiferromagnetic substrate. *J. Appl. Phys.* **62**, 3047–3049 (1987).

[15] Koon, N. C. Calculations of exchange bias in thin films with ferromagnetic/antiferromagnetic interfaces. *Phys. Rev. Lett.* **78**, 4865–4868 (1997).

[16] Schulthess, T. & Butler, W. Consequences of spin-flop coupling in exchange biased films. *Phys. Rev. Lett.* **81**, 4516–4519 (1998).

[17] Schulthess, T. & Butler, W. Coupling mechanisms in exchange biased films (invited). *J. Appl. Phys.* **85**, 5510–5515 (1999).

[18] Nowak, U., Misra, A. & Usadel, K. Domain state model for exchange bias. *J. Appl. Phys.* **89**, 7269–7271 (2001).

[19] Nowak, U. *et al.* Domain state model for exchange bias. I. Theory. *Phys. Rev. B* **66**, 014430 (2002).

[20] Radu, F. *Fundamental aspects of exchange bias effect* (Ruhr- University Bochum, 2005).

[21] Radu, F., Westphalen, A., Theis-Brohl, K. & Zabel, H. Quantitative description of the azimuthal dependence of the exchange bias effect. *J. Phys.:Condens. Matter* **18**, L29–L36 (2006).

[22] Radu, F. & Zabel, H. *Springer tracts in modern physics*, vol. 227 (Springer, 2008).

[23] Ravelosona, D., Chappert, C., Mathet, V. & Bernas, H. Chemical order induced by ion irradiation in FePt (001) films. *Appl. Phys. Lett.* **76**, 236–238 (2000).

[24] Ravelosona, D., Chappert, C., Mathet, V. & Bernas, H. Chemical order induced by He^+ ion irradiation in FePt(001) films. *J. Appl. Phys.* **87**, 5771–5773 (2000).

[25] Lai, C., Yang, C. & Chiang, C. Ion-irradiation-induced direct ordering of $L1_0$ FePt phase. *Appl. Phys. Lett.* **83**, 4550–4552 (2003).

[26] Bernas, H. *et al.* Ordering intermetallic alloys by ion irradiation: A way to tailor magnetic media. *Phys. Rev. Lett.* **91**, 077203 (2003).

[27] Maeda, T., Kai, T., Kikitsu, A., Nagase, T. & Akiyama, J. Reduction of ordering temperature of an FePt-ordered alloy by addition of Cu. *Appl. Phys. Lett.* **80**, 2147–2149 (2002).

[28] Lee, S., Yang, S., Kim, Y. & Na, J. Rapid ordering of Zr-doped FePt alloy films. *Appl. Phys. Lett.* **78**, 4001–4003 (2001).

[29] Coffey, K., Parker, M. & Howard, J. High anisotropy $L1_0$ thin films for longitudinal recording. *IEEE Trans. on Mag.* **31**, 2737–2739 (1995).

[30] Lai, C., Wu, Y. & Chiang, C. Effects of forming gas annealing on low-temperature ordering of FePt films. *J. Appl. Phys.* **97**, 10H305 (2005).

[31] Chen, S. *et al.* Improvement in hard magnetic properties of FePt films by introduction of Ti underlayer. *IEEE Trans. on Mag.* **41**, 915–917 (2005).

[32] Hsu, Y., Jeong, S., Laughlin, D. & Lambeth, D. Effects of Ag underlayers on the microstructure and magnetic properties of epitaxial FePt thin films. *J. Appl. Phys.* **89**, 7068–7070 (2001).

[33] Hsu, Y., Jeong, S., Laughlin, D. & Lambeth, D. The effects of Ag underlayer and Pt intermediate layers on the microstructure and magnetic properties of epitaxial FePt thin films. *JMMM* **260**, 282–294 (2003).

[34] Xu, Y., Chen, J. & Wang, J. In situ ordering of FePt thin films with face-centered-tetragonal (001) texture on $Cr_{100-x}Ru_x$ underlayer at low substrate temperature. *Appl. Phys. Lett.* **80**, 3325–3327 (2002).

[35] Chen, J., Lim, B. & Wang, J. Controlling the crystallographic orientation and the axis of magnetic anisotropy in $L1_0$ FePt films. *Appl. Phys. Lett.* **81**, 1848–1850 (2002).

[36] Lai, C., Yang, C., Chiang, C., Balaji, T. & Tseng, T. Dynamic stress-induced low-temperature ordering of FePt. *Appl. Phys. Lett.* **85**, 4430–4432 (2004).

[37] Moser, A. *et al.* Magnetic recording: advancing into the future. *J. Phys. D* **35**, R157–R167 (2002).

[38] Ko, H., Perumal, A. & Shin, S. Fine control of $L1_0$ ordering and grain growth kinetics by C doping in FePt films. *Appl. Phys. Lett.* **82**, 2311–2313 (2003).

[39] Yan, M. *et al.* Fabrication of nonepitaxially grown double-layered FePt : C/FeCoNi thin films for perpendicular recording. *Appl. Phys. Lett.* **83**, 3332–3334 (2003).

[40] Perumal, A., Takahashi, Y. K. & Hono, K. $L1_0$ FePt-C nanogranular perpendicular anisotropy films with narrow size distribution. *Appl. Phys. Exp.* **1**, 101301 (2008).

[41] Perumal, A., Takahashi, Y. K. & Hono, K. FePt-C nanogranular films for perpendicular magnetic recording. *J. Appl. Phys.* **105**, 07B732 (2009).

[42] Luo, C., Liou, S., Gao, L., Liu, Y. & Sellmyer, D. Nanostructured FePt : B_2O_3 thin films with perpendicular magnetic anisotropy. *Appl. Phys. Lett.* **77**, 2225–2227 (2000).

[43] Ichitsubo, T. *et al.* Mechanism of c-axis orientation of $L1_0$ FePt in nanostructured FePt/B_2O_3 thin films. *Phys. Rev. B* **77**, 094114 (2008).

[44] Pike, C., Roberts, A. & Verosub, K. Characterizing interactions in fine magnetic particle systems using first order reversal curves. *J. Appl. Phys.* **85**, 6660–6667 (1999).

[45] Preisach, F. Über die magnetische nachwirkung. *Z. Phys.* **94**, 277–302 (1935).

[46] Pike, C. First-order reversal-curve diagrams and reversible magnetization. *Phys. Rev. B* **68**, 104424 (2003).

[47] Pike, C., Roberts, A., Dekkers, M. & Verosub, K. An investigation of multi-domain hysteresis mechanisms using FORC diagrams. *Phys. Earth Planet. Inter.* **126**, 11–25 (2001).

[48] Thole, B. T., Carra, P., Sette, F. & van der Laan, G. X-ray circular dichroism as a probe of orbital magnetization. *Phys. Rev. Lett.* **68**, 1943–1946 (1992).

[49] Maesaka, A., Ishii, S. & Okabe, A. Transmission electron microscopy analysis of crystallographic transition from fcc to fct on PtMn spin valves. *J. Appl. Phys.* **88**, 3982–3987 (2000).

[50] Gao, Y., Wang, Z. & Whang, S. Deformation behavior in $L1_0$-type FePt compound. *Mater. Sci. Eng. A* **192**, 53–58 (1995).

[51] Meyer, G. & Thiele, J. Effective electron-density dependence of the magnetocrystalline anisotropy in highly chemically ordered pseudobinary $(Fe_{1-x}Mn_x)_{50}Pt_{50}$ $L1_0$ alloys. *Phys. Rev. B* **73**, 214438 (2006).

[52] Menshikov, A., Antropov, V., Gasnikova, G., Dorofeyev, Y. & Kazantsev, V. Magnetic phase-diagram of ordered $(Fe_{1-X}Mn_X)Pt$ alloys. *J. Magn. Magn. Mater* **65**, 159–166 (1987).

[53] Lai, C. & Ho, C. Improvement of magnetic properties of FePt nanoparticles by adding Mn. *J. Appl. Phys.* **97**, 10J314 (2005).

[54] Weisheit, M., Schultz, L. & Fahler, S. Textured growth of highly coercive $L1_0$ ordered FePt thin films on single crystalline and amorphous substrates. *J. Appl. Phys.* **95**, 7489–7491 (2004).

[55] Davies, J. E., Hellwig, O., Fullerton, E. E. & Liu, K. Temperature-dependent magnetization reversal in (Co/Pt)/Ru multilayers. *Phys. Rev. B* **77**, 014421 (2008).

[56] Suess, D. Multilayer exchange spring media for magnetic recording. *Appl. Phys. Lett.* **89**, 113105 (2006).

[57] Suess, D., Fidler, J., Zimanyi, G., Schrefl, T. & Visscher, P. Thermal stability of graded exchange spring media under the influence of external fields. *Appl. Phys. Lett.* **92**, 173111 (2008).

[58] Zimanyi, G. T. Graded media: Optimization and energy barriers (invited). *J. Appl. Phys.* **103**, 07F543 (2008).

[59] Suess, D., Lee, J., Fidler, J. & Schrefl, T. Exchange-coupled perpendicular media. *J. Magn. Magn. Mater* **321**, 545–554 (2009).

[60] Majkrzak, C. Polarized neutron reflectometry. *Physica B* **173**, 75–88 (1991).

[61] Moon, R., Riste, T. & Koehler, W. Polarization analysis of thermal-neutron scattering. *Phys. Rev.* **181**, 920 (1969).

[62] Kirby, B. J. *et al.* Vertically graded anisotropy in Co/Pd multilayers. *Phys. Rev. B* **81**, 100405 (2010).